Large-eddy simulations of turbulent flow in a rotating square duct

J. Pallares[a] and L. Davidson[b]
Department of Thermo and Fluid Dynamics, Chalmers University of Technology, 412 96 Gothenburg, Sweden

(Received 15 July 1999; accepted 21 July 2000)

The turbulent flow at low Reynolds numbers in a rotating straight square duct was simulated using the large-eddy simulation technique. The rotation axis is parallel to two opposite walls of the duct, and the pressure-driven flow is assumed to be fully developed, isothermal and incompressible. The Reynolds number based on the friction velocity ($Re_\tau=300$) was kept constant in the range of the rotational numbers studied ($0\leqslant Ro_\tau\leqslant 1.5$) Computations were carried out using a second-order finite volume code with a localized one-equation dynamic subgrid scale model. Simulations of rotating channel flows were initially carried out and were seen to be in agreement with experiments and direct numerical simulations reported in the literature. The study of the flow in a rotating square duct revealed the influence of the Coriolis force on the spatial distribution of the average velocity fields and Reynolds stresses. At low rotation rates, turbulence-driven secondary flows developed near the corners convect the rotation-generated cross-stream currents. At moderate and high rotation rates, the mean secondary flow structure consists essentially of two large counter-rotating cells convecting low/high momentum fluid from the stable/unstable side to the unstable/stable side. Inspection of the terms of the transport equations of the average axial velocity and vorticity components shows the mechanisms responsible for the changes in the average flow structure. Spatial distributions of the Reynolds stresses are mainly influenced by the changes that rotation induces in the main strain rates. It has been found that, globally, at the low Reynolds number studied, rotation tends to significantly reduce the overall turbulence level of the flow. © *2000 American Institute of Physics.* [S1070-6631(00)51011-3]

I. INTRODUCTION

Rotation effects in wall-bounded flows appear in many natural and engineering situations. The prediction of flow in rotating devices and, particularly, demanding blade cooling technology for industrial and aircraft turbines have motivated many of the existing studies dealing with rotating channel or duct flows. Fluid flow in most of these circumstances is turbulent, and the coupling of the rotation-induced forces on a turbulence structure has been extensively studied in two-dimensional channels.

Physical phenomena occurring in turbulent channel flows subjected to rotation around an axis parallel to the spanwise direction have been investigated experimentally[1] and numerically.[2–7] Two main features arise when the axis of rotation is perpendicular to the plane of mean shear. First, it is well established that the interaction of the Coriolis force with the mean shear produces stabilization or destabilization of the flow near the two walls. Here, the concept of stability is related to an increase (destabilization) or with a decrease (stabilization) of the turbulence levels with respect to the nonrotating case. On the unstable side (or pressure side) of the channel, the mean shear vorticity is parallel to the rotation vector while, on the stable side (or suction side), these two vectors are anti-parallel. This situation can lead to the complete suppression of turbulence and the relaminarization of the flow on the stable side of the channel if the rotation rate is sufficiently high. A second effect of rotation is the development of longitudinal large-scale counter-rotating roll cells. These Taylor–Görtler vortices, analogous to those that develop due to the centrifugal instability arising from the streamline curvature, are localized on the unstable side but tend to drift along the spanwise and cross-stream directions and convect high momentum fluid towards the stable side.

Turbulent flow in a nonrotating duct with a rectangular cross-section is of engineering interest. It also has structurally remarkable features, especially near the corners where the flow has two inhomogeneous directions and where, on average, secondary flows of second kind develop. The mean structure of these flows in a cross-section of the duct consists of eight counter-rotating vortices which are distributed in pairs in the four quadrants and convect high momentum fluid from the central region of the duct to the corner region along the corner bisector. Low Reynolds number computations[8–10] show that secondary flows are relatively weak, with a maximum of 2%–3% of the mean axial velocity, but contribute considerably to the wall stress distributions. Huser and Biringen[10] proposed an explanation of the mechanism for the generation of secondary flows based on quadrant analysis carried out with direct numerical simulations (DNS) data. According to these authors, the bursting events in the corners are suppressed by the reduced mean shear in the corner bi-

[a]Present address: Department of Mechanical Engineering, University Rovira Virgili, 43007-Tarragona, Spain.
[b]Author to whom correspondence should be addressed. Electronic mail: lada@tfd.chalmers.se; telephone: +46 317721404; fax +46 31180976.

 © 2000 American Institute of Physics

Downloaded 19 Sep 2001 to 129.16.64.43. Redistribution subject to AIP license or copyright, see http://ojps.aip.org/phf/phfcr.jsp

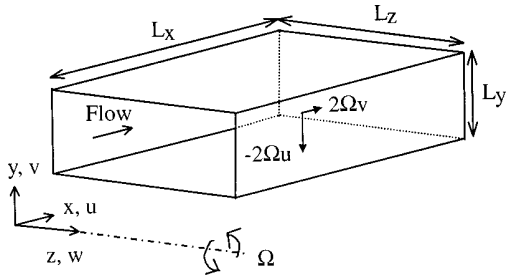

FIG. 1. Physical model and coordinate system.

sector. This, together with the fact that ejections of low momentum fluid from the walls generate a pair of streamwise counter-rotating vortices, results in the situation that the sense of rotation of the vortex closer to the corner determines the sense of rotation of the secondary circulation in that octant.

Rotating rectangular duct flow in a laminar regime was studied experimentally by Hart[11] and numerically by Speziale[12] and Speziale and Thangam.[13] In these works a similar evolution of the flow as the rotation rate, parallel to the longest side of the duct, was increased was reported. At weak rotation rates, the axial velocity profile along the direction of rotation is quasi-parabolic and a double-vortex structure appears near the shortest walls of the duct. At intermediate rotation rates, an instability in the form of longitudinal roll cells was observed. In this case, the profile of the streamwise velocity was distorted with a wavy structure by the presence of the rolls. At more rapid rotation rates, the restabilization of the flow to a Taylor–Proudman regime occurred (i.e., the axial velocity does not vary along the direction of the axis of rotation). The roll cells disappear, and a stretched double-vortex secondary flow appears which is quite similar to the one previous to the onset of instability.

The present study analyzes turbulent rotating square duct flows at low Reynolds ($\mathrm{Re}_\tau=300$) and rotation numbers ($0 \leqslant \mathrm{Ro}_\tau \leqslant 1.5$). To our knowledge, there is no previous numerical work dealing with the effect of rotation on turbulence-driven secondary flows. The large-eddy simulation (LES) technique was chosen to keep the computational requirements at a moderate level. Previous numerical studies carried out to simulate turbulent flows in nonrotating ducts[8] and flows in rotating channel flow[3,4] showed the capability of the LES approach to give accurate results in these flows. The localized one-equation dynamic subgrid scale (SGS) model proposed recently by Kim and Menon[14] was used in the present computations. More details on the SGS model are given in Sec. II, where the physical and mathematical models are described. Validation of the simulations in rotating channel flow is reported in Sec. III. Results of the simulations of the rotating square duct flow simulations are presented and discussed in Sec. IV.

II. MODEL

Figure 1 shows the physical model of the plane channel ($L_z=\infty$) and the straight square duct ($L_z=L_y$). The flow, driven by an externally imposed mean pressure gradient, is assumed to be fully developed, incompressible and isothermal. The two walls of the infinite channel ($y=-L_y/2$ $y=L_y/2$) and the four walls of the duct ($y=0, y=L_y$, $z=0, z=L_z$) are rigid and smooth. The entire system is rotating with respect to a fixed frame of reference with a constant positive angular velocity parallel to the z direction, $\vec{\Omega}=(0,0,\Omega)$. Directions of the two components of the Coriolis force are indicated in Fig. 1.

The large-eddy simulation technique is based on decomposition of the flow variables into a large-scale component (or resolved) and a subgrid scale component. The resolved scales, denoted with an overbar, and the corresponding governing transport equations are defined by the filtering operation.[15] The nondimensional filtered Navier–Stokes and continuity equations are

$$\frac{\partial \bar{u}_i}{\partial t}+\frac{\partial \bar{u}_i\bar{u}_j}{\partial x_j}=-\left(\delta_{1j}\frac{\partial P}{\partial x_i}+\frac{\partial \bar{p}}{\partial x_i}\right) -\frac{\partial \tau_{ij}}{\partial x_j}+\frac{1}{\mathrm{Re}_\tau}\frac{\partial^2 \bar{u}_i}{\partial x_j \partial x_j}+\epsilon_{ij3}\mathrm{Ro}_\tau \bar{u}_j \tag{1}$$

and

$$\frac{\partial \bar{u}_i}{\partial x_i}=0, \tag{2}$$

respectively. The scales used to obtain the nondimensional variables are the channel half-width ($D=L_y/2$) and the hydraulic diameter ($D=L_y$) as length scales for channel and square duct flow, respectively, and the average friction velocity (u_τ). Pressure has been scaled with the average wall stress, ρu_τ^2. In Eq. (1), $\in_{ij3}$ is the Levi-Civita's alternating tensor, $\mathrm{Re}_\tau=u_\tau D/\nu$ and $\mathrm{Ro}_\tau=2\Omega D/u_\tau$ are the Reynolds and the rotational numbers, respectively, and $\delta_{1j}\,dP/dx_i$ is the imposed mean pressure gradient along the streamwise direction ($dP/dx=-1$ for channel flow and $dP/dx=-4$ for duct flow).

In the present work, the subgrid scale stresses (τ_{ij}) have been computed following the localized one-equation dynamic SGS model developed by Kim and Menon.[14] A brief description of the model is given in the following. The SGS stress tensor is modeled as

$$\tau_{ij}=-2C_\tau \bar{\Delta} k_{\mathrm{SGS}}^{1/2}\bar{S}_{ij}+\tfrac{1}{3}\delta_{ij}\tau_{kk}, \tag{3}$$

where C_τ is a coefficient to be computed dynamically, $\bar{\Delta}$ is the characteristic subgrid scale energy length (or grid scale), k_{SGS} is the subgrid scale kinetic energy and $\bar{S}_{ij}$ is the resolved strain tensor. The second term on the right-hand side of Eq. (3) is included in the pressure term. The subgrid scale kinetic energy (k_{SGS}) is obtained by solving its transport equation (see Ref. 14), in which the dissipation term (ϵ_{SGS}) is modeled as

$$\epsilon_{\mathrm{SGS}}=\frac{C_\epsilon k_{\mathrm{SGS}}^{3/2}}{\bar{\Delta}}, \tag{4}$$

where C_ϵ is another coefficient also determined dynamically.

The procedure for computing the localized values of the model coefficients, C_τ and C_ϵ, is based, as in other localized

Downloaded 19 Sep 2001 to 129.16.64.43. Redistribution subject to AIP license or copyright, see http://ojps.aip.org/phf/phfcr.jsp

TABLE I. Characteristics of direct[a] and large-eddy numerical simulations.

	Authors	Grid points $x \quad y \quad z$	Domain $Lx\ Ly\ Lz$	Re_τ $(u_\tau D/\nu)$	Ro_τ $(2\Omega D/u_\tau)$
Channel	Kristoffersen and Andersson (Ref. 5)[a]	128×128×128	$4\pi\times2\times2\pi$	194	$-7.5\leqslant \mathrm{Ro}_\tau \leqslant 0$
	Alvelius (Ref. 7)[a]	384×129×240	$8\pi\times2\times3\pi$	180	$0.1\leqslant \mathrm{Ro}_\tau \leqslant 7.3$
	Present	66×66×66	$4\pi\times2\times\pi$	194	0.15,1.5,3.6
Duct	Present	66×66×66	$2\pi\times1\times1$	300	$0\leqslant \mathrm{Ro}_\tau \leqslant 1.5$

dynamic SGS models,[15] on the definition of a test scale field. The test filter, characterized by $\hat{\Delta}$ and equal to $2\bar{\Delta}$, and applied to any variable $\bar{\phi}$, is denoted by $\hat{\phi}$. The experimentally measured similarity[16] between the dynamic Leonard stresses, $L_{ij}=(\widehat{\bar{u}_i\bar{u}_j}-\hat{\bar{u}}_i\hat{\bar{u}}_j)$, and the SGS stresses allows a reasonable assumption of the same parametrization for both tensors, τ_{ij} and L_{ij},

$$L_{ij}=-2C_\tau\hat{\Delta}k_{\mathrm{test}}^{1/2}\hat{\bar{S}}_{ij}+\tfrac{1}{3}\delta_{ij}L_{kk}, \tag{5}$$

where k_{test} is the resolved kinetic energy at the test scale. The over-determined model coefficient C_τ in Eq. (5) can be computed from resolved quantities at the test filter level, using the least-square minimization procedure,

$$C_\tau=\frac{1}{2}\frac{L_{ij}\hat{\bar{S}}_{ij}}{\hat{\bar{S}}_{ij}\hat{\bar{S}}_{ij}}. \tag{6}$$

The dissipation rate of the test scale kinetic energy at the small scales is produced by the molecular (ν) and the SGS viscosity (ν_T) and can be written as

$$\epsilon_{\mathrm{test}}=(\nu+\nu_T)\left[\left(\widehat{\frac{\partial\bar{u}_i}{\partial x_j}\frac{\partial\bar{u}_i}{\partial x_j}}\right)-\left(\frac{\partial\hat{\bar{u}}_i}{\partial x_j}\frac{\partial\hat{\bar{u}}_i}{\partial x_j}\right)\right]. \tag{7}$$

The similarity between the dissipation rates at the grid filter level (ϵ_{SGS}) and the test filter level (ϵ_{test}) is also invoked, and the dissipation model coefficient (C_ϵ) is computed as

$$C_\epsilon=\frac{\hat{\Delta}\epsilon_{\mathrm{test}}}{k_{\mathrm{test}}^{3/2}}. \tag{8}$$

This model, based on the similarity between the SGS stress tensor and the dynamic Leonard stress tensor, overcomes the numerical stability problems of the earlier dynamic models without any averaging or adjustment of the model coefficients because the denominators of Eqs. (6) and (8) have well defined quantities. This is an important feature when simulating turbulent flows under rotation because of the stabilizing/destabilizing effects of rotation on turbulence. Kim and Menon[14] examined the properties of the model by conducting LES of turbulent flows such as decaying, forced and rotating isotropic turbulence, turbulent mixing layer and plane Couette flow. Their results showed good agreement with existing experimental and DNS data.

The governing transport equations [Eqs. (1) and (2)] were solved numerically with the CALC-LES code.[17,18] This second-order accuracy finite volume code uses central differencing of the diffusive and convective terms on a collocated grid and a Crank–Nicolson scheme for the temporal discretization. The coupling between the velocity and pressure fields is solved efficiently by means of an implicit, two-step, time advancement method and a multigrid solver for the resulting Poisson equation. This code has several optional SGS models implemented and has been successfully tested in simulating various transitional and turbulent flows of engineering interest such as flow around obstacles[19–21] and buoyancy-driven and forced convection recirculating flows in enclosures.[18,22]

Table I summarizes the characteristics of present simulations and DNS of rotating channel flows used for validation. The computational domain was divided into $66\times66\times66$ grid nodes. They were uniformly distributed along the homogeneous directions ($\Delta x^+\approx37$ and $\Delta z^+\approx9$ for the channel and $\Delta x^+\approx29$ for the square duct) in which periodic boundary conditions were imposed, while tanh distributions were used to stretch the nodes near the walls where the no-slip condition was applied. For the Reynolds numbers considered, the minimum and maximum grid spacing in the directions perpendicular to the walls are $(\Delta y^+)_{\min}\approx0.7$ and $(\Delta y^+)_{\max}\approx11$ for the channel flow ($\mathrm{Re}_\tau=194$) and $(\Delta y^+)_{\min}\approx(\Delta z^+)_{\min}\approx0.4$ and $(\Delta y^+)_{\max}=(\Delta z^+)_{\max}\approx9$ for the square duct flow ($\mathrm{Re}_\tau=300$).

The sampling procedure used to obtain the average velocity fields and the turbulent intensities was not started until the flow was fully developed. The flow quantities were averaged along the homogeneous directions as well as in time, typically over about 15 and 40–70 nondimensional time units for channel and duct flows, respectively. Results at the lowest rotation rates were obtained starting from the nonrotating flow fields until a new statistically steady state was reached. The rotation number was successively increased maintaining a constant imposed pressure gradient (i.e., a constant value of Re_τ). The computed mean wall stress (τ_w) is balanced by the imposed pressure gradient within 0.05% in all the simulations reported in this work. In the following discussions, the averaged resolved velocities and turbulent stresses are denoted U_i and $\langle u_i'u_j'\rangle$ for simplicity.

III. VALIDATION

Before the results of the simulation of the rotating square duct are presented in the next section, it is of interest to compare and validate the averaged velocity fields and some of the primary statistics obtained in the present simulations of rotating channel flows. Computations of stationary chan-

Downloaded 19 Sep 2001 to 129.16.64.43. Redistribution subject to AIP license or copyright, see http://ojps.aip.org/phf/phfcr.jsp

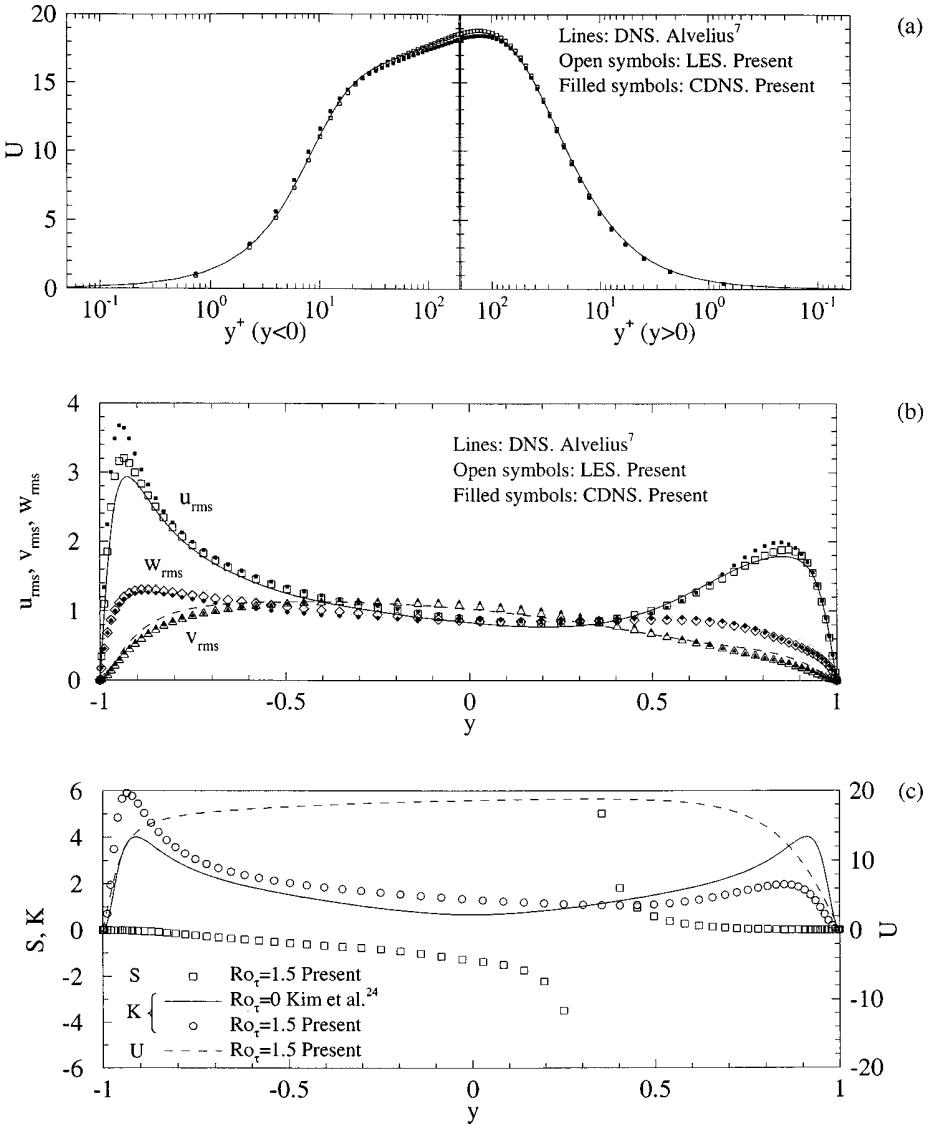

FIG. 2. Mean velocity (a) and turbulence intensity (b) profiles in a rotating channel at $\mathrm{Re}_\tau=180$, $\mathrm{Ro}_\tau=1.8$ [Alvelius (Ref. 7)] and $\mathrm{Re}_\tau=194$, $\mathrm{Ro}_\tau=1.5$. Vertical profiles of the parameter S and the average kinetic energy in nonrotating and rotating channel flow (c).

nel and duct flows were initially carried out and results[23] were seen to be in agreement with existing numerical and experimental data.

Figures 2(a) and 2(b) show the mean streamwise velocity and turbulence intensity vertical profiles of rotating channel flow at $\mathrm{Ro}_\tau=1.5$, respectively. Results of a coarse direct numerical simulation (CDNS) without any SGS model on the same grid and flow conditions as the LES are plotted in Figs. 2(a) and 2(b) for comparison. The DNS of Alvelius[7] at $\mathrm{Ro}_\tau=1.8$ was selected for the comparison because the computational domain used by this author is the largest of the rotating channel flow studies shown in Table I and has the same grid resolution as the DNS of Kim *et al.*[24] Good agreement is found when comparing, in Figs. 2(a) and 2(b), the DNS of Alvelius[7] and the present LES. It can be seen in Figs. 2(a) and 2(b) that the SGS model has beneficial effects in predicting both averaged velocities and Reynolds stresses. Differences between averaged velocities predicted by the present LES and the DNS of Alvelius are less than 1% in the buffer and log layers while predictions of the CDNS differ about 2%–5% from the DNS. The benefits of the SGS model are more evident when comparing in Fig. 2(b) the predictions of the near-wall peak of the main normal stress. Present LES and CDNS overpredict the maximum value of u_{rms} by 12% and 30%, respectively.

As shown in Fig. 2(a), the average velocity profile becomes asymmetric under the effect of rotation. The normal Reynolds stresses are generally reduced in comparison with the nonrotating case on the stable side (near the stable wall, $y=1$) and increased on the unstable side (near the unstable wall, $y=-1$). Detailed analyses of the effects of rotation on the different Reynolds stresses based on the generation terms of the transport equations, are reported in Johnston *et al.*[1] and Kristoffersen and Andersson.[5]

According to Johnston *et al.*,[1] the stabilizing or destabilizing effect of rotation (i.e., the tendency to decrease or increase the turbulent kinetic energy) can be determined with the parameter S defined as the ratio of the background vorticity (Ro_τ) to the mean shear vorticity ($-dU/dy$).

Figure 2(c) shows the profiles of S and U at $\mathrm{Ro}_\tau=1.5$ and the turbulent kinetic energy, $K=[\langle u'^2\rangle+\langle v'^2\rangle+\langle w'^2\rangle]/2$, at $\mathrm{Ro}_\tau=0$ and $\mathrm{Ro}_\tau=1.5$. The present LES accu-

Downloaded 19 Sep 2001 to 129.16.64.43. Redistribution subject to AIP license or copyright, see http://ojps.aip.org/phf/phfcr.jsp

rately reproduce the quasi-linear region of the profile of U, where the absolute mean vorticity, $(-dU/dy)+\mathrm{Ro}_\tau$, becomes approximately zero (i.e., $dU/dy \approx \mathrm{Ro}_\tau$). However, it can be seen that S decreases monotonically in the range of $-1<y<0$ and there is thus no noticeable region in which $S=-1$. As pointed out by Johnston *et al.*,[1] the profiles of K [Fig. 2(c)] indicate that the effect of rotation is destabilizing (an increase in K with respect to the nonrotating case) when $S<0 (-1=y<0.3)$ and stabilizing (a decrease in K) when $S>0 (0.3<y=1)$. This supports the idea that the position of the maximum of U ($dU/dy=0$ and $S \rightarrow \pm\infty$) can be used as a boundary between the stable and unstable side of the channel.

Taylor–Görtler vortices have been observed in the present simulations at $\mathrm{Ro}_\tau=1.5$ and $\mathrm{Ro}_\tau=3.6$. Kristoffersen and Andersson[5] observed that if the ratio between the spanwise dimension of the computational domain and the preferred wavelength of these vortices at a given rotation rate is not close to an integer value, they drift laterally because of the periodic boundary conditions applied in the spanwise direction. In this situation, time and streamwise averaging tend to blur the detection of these structures in a mean cross-stream flow field. In agreement with Kristoffersen and Andersson,[5] at $\mathrm{Ro}_\tau=1.5$ and $L_z \approx 3.1$, a pair of fairly persistent counter-rotating vortices were observed in a mean cross-stream flow field averaged up to 5 nondimensional time units or letots (large-eddy turnover time). At $\mathrm{Ro}_\tau=3.6$, inspection of some of the present instantaneous and short-term averaged flow fields revealed that large-scale vortices with a wavelength of about 2.7 tend to drift along the spanwise direction. In fact, a simulation carried out with $L_z=2.75$ ($\Delta z^+ \approx 9$) revealed that, at $\mathrm{Ro}_\tau=3.6$, a pair of vortices is detected in the mean cross-stream flow field averaging up to 15 letots. As expected, the turbulence intensities profiles shown in Fig. 2(b) are not affected by the presence of a persistent roll configuration owing to the spanwise averaging.

Figure 3 shows mean local wall friction velocities scaled with the average friction velocity at the stable ($u_\tau<1$) and unstable ($u_\tau>1$) walls of a rotating channel as a function of the rotation number Ro ($\mathrm{Ro}=\mathrm{Ro}_\tau u_\tau/U_b$). Considerable scatter can be seen at both walls. In the experiments of Johnston *et al.*,[1] the bulk velocity was obtained from the volume flow rate. This led to an overestimation of the rotation number, shifting their data, plotted in Fig. 3, slightly to the right. Average friction velocities in a rotating square duct are also included in Fig. 3 but are discussed in the next section. The present predictions of the local friction velocities at $\mathrm{Ro}=9.4\times10^{-3}$ ($\mathrm{Ro}_\tau=0.15$), 8.9×10^{-2} ($\mathrm{Ro}_\tau=1.5$) and 0.23 ($\mathrm{Ro}_\tau=3.6$) are in agreement with the DNS and LES data plotted in Fig. 3. It can be seen that, at low rotation numbers ($\mathrm{Ro}<0.03$) Miyake and Kajishima[2] and Tafti and Vanka[3] who used Smagorinsky SGS models overpredict/underpredict the friction velocities at the unstable/stable wall, while their results show better agreement with other DNS and LES at higher rotational numbers ($\mathrm{Ro}>0.05$).

IV. RESULTS AND DISCUSSION

In this section we present the results of the simulations of the turbulent rotating square duct flow. Changes in the topology of the mean velocity fields as the rotation rate is increased are described in Sec. IV A and analyzed in Sec. IV B. Effects of rotation on the primary turbulence statistics are analyzed with consideration to the generation terms of the transport equations for the Reynolds stress components in Sec. IV C. Predictions of wall friction velocities are discussed and compared with rotating channel flow data in Sec. IV D. Computed terms of the mean streamwise vorticity transport equation are presented and discussed in Sec. IV E in order to determine the mechanisms responsible for the changes in the secondary flow structure as the rotation rate is increased. Finally, in Sec. IV F we present some visualizations of the instantaneous streamwise vortices in the flow.

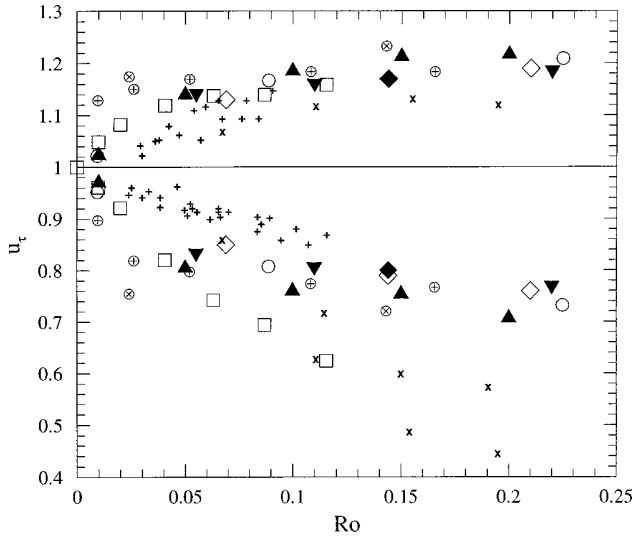

FIG. 3. Averaged local wall friction velocities at the top and bottom walls as a function of Ro. $u_{\tau s} \leqslant 1$, stable side wall; $u_{\tau u} \geqslant 1$, unstable side wall. Rotating channel flow: +, Re≈5500; ×, Re≈18000, Johnston *et al.* (Ref. 1); ⊕, LES, Miyake and Kajishima (Ref. 2); ⊗, LES, Tafti and Vanka (Ref. 3); ▲, DNS, Kristoffersen and Andersson (Ref. 5); ◆, DNS; ◇, LES, Piomelli and Liu (Ref. 4); ▼, Alvelius (Ref. 7) ○, Present. Rotating square duct □, present.

Rotating square duct flow at $\mathrm{Re}_\tau=300$ was simulated at six different rotational numbers, $\mathrm{Ro}_\tau=0.15$ ($\mathrm{Ro}=0.0099$), $\mathrm{Ro}_\tau=0.3$ ($\mathrm{Ro}=0.020$), $\mathrm{Ro}_\tau=0.6$ ($\mathrm{Ro}=0.041$), $\mathrm{Ro}_\tau=0.9$ ($\mathrm{Ro}=0.063$), $\mathrm{Ro}_\tau=1.2$ ($\mathrm{Ro}=0.087$) and $\mathrm{Ro}_\tau=1.5$ ($\mathrm{Ro}=0.12$). Time and x-direction averaged flows progressively tend to be symmetric with respect to the horizontal wall bisector $z=0.5$ as the sampling time is increased. Consequently, the flow was averaged with respect to $z=0.5$ to increase the sampling size. At high rotation rates, long-term simulations of about 70 letots were required to obtain symmetric velocity fields to within 3%.

A. Mean flow fields

Figures 4(a) to 4(f) show the mean velocity fields (contours of the streamwise velocity component together with the cross-stream vectors). In these figures only half the vectors in each direction are shown. It can be seen that the general effects on the distributions of the mean streamwise velocity component as the (positive) rotation rate is increased are the reduction of the axial velocity near the stable wall ($y=1$), the displacement of the maximum towards the unstable wall

Downloaded 19 Sep 2001 to 129.16.64.43. Redistribution subject to AIP license or copyright, see http://ojps.aip.org/phf/phfcr.jsp

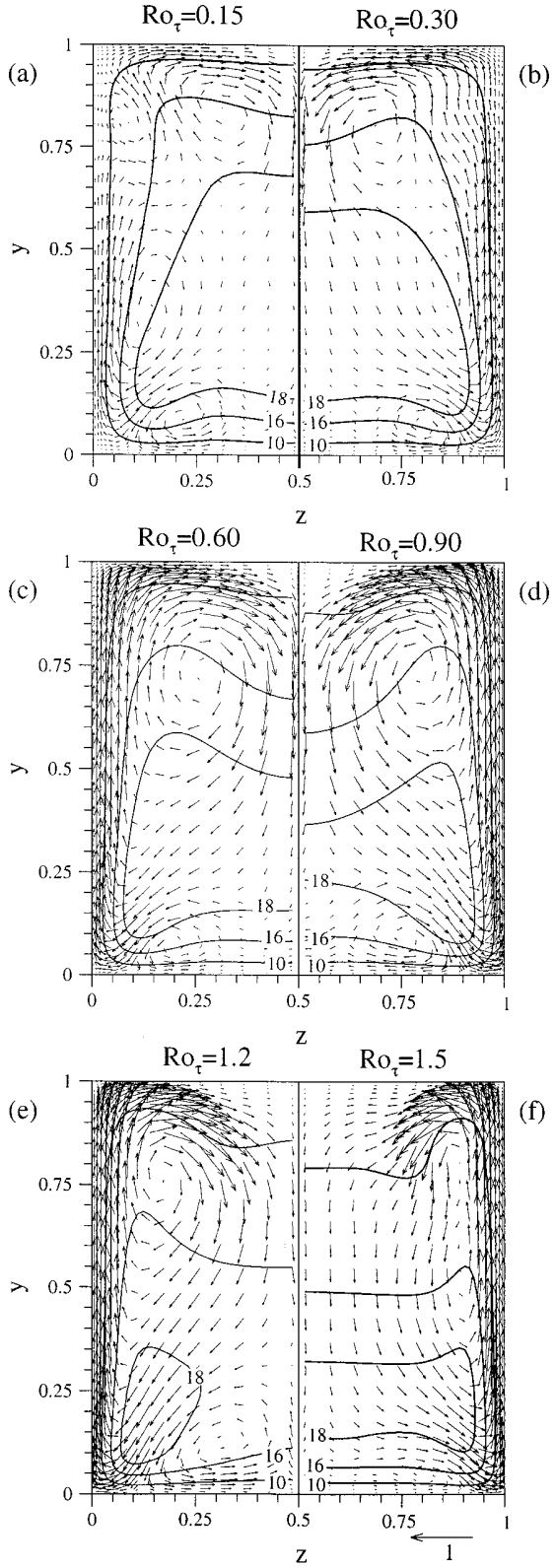

FIG. 4. Rotating square duct resolved mean flow field averaged in half of the cross-section at $Re_\tau=300$. (a) $Ro_\tau=0.15$, (b) $Ro_\tau=0.30$, (c) $Ro_\tau=0.60$, (d) $Ro_\tau=0.90$, (e) $Ro_\tau=1.2$, and (f) $Ro_\tau=1.5$. Contours of the axial velocity component together with the cross-stream vector field.

($y=0$) and towards the sidewalls. There is an overall reduction of the axial flow rate if, as in the present computations, the imposed mean pressure gradient is kept constant. For example, the axial flow rate is reduced, compared to the nonrotating case, by about 2% at $Ro_\tau=0.6$ and 14% at $Ro_\tau=1.5$.

The right-hand side Coriolis term in the y-momentum equation ($-Ro_\tau u$) produces a secondary descending flow that convects low momentum fluid from the stable side (near $y=1$) across the central part of the duct, where the streamwise velocity is larger, to the unstable side (near $y=0$). The corresponding ascending currents occur in narrow regions near the sidewalls ($z=0$ and $z=1$), where the streamwise velocity and thus the vertical component of the Coriolis force is smaller than in the center of the duct. Figures 4(a) ($Ro_\tau=0.15$) and 4(b) ($Ro_\tau=0.3$) show how turbulence-driven secondary flows are affected by low rotation rates. It can be seen that the cross-stream flows become asymmetric with respect to the corner bisectors. The secondary flows near the unstable wall ($y=0$) convect the Coriolis-generated vertical descending current to the bottom corners [Figs. 4(a) and 4(b)]. The increase in the cross-stream recirculating flow rate, compared to the nonrotating case, produces the enlargement of the secondary flows located over the bottom corner bisectors. At $Ro_\tau=0.15$ [Fig. 4(a)], the ascending vertical flow near the side wall $z=0$ is convected towards the top wall bisector by the clockwise rotating secondary flow of the top left quadrant of the duct. There is a considerable reduction, as compared to the nonrotating case,[23] of the secondary cell below the top corner bisector. Figure 4(b) shows that, at $Ro_\tau=0.3$, this secondary flow cell has disappeared altogether. The enlarged secondary cells near the side and top walls, shown in Fig. 4(a), merge in the range of $0.30<Ro_\tau<0.6$. It can be seen in Figs. 4(c) to 4(f) that the mean cross-stream flow fields at $Ro_\tau\geqslant 0.6$ are constituted by two counter-rotating secondary flows. The centers of the larger cells are located on the stable side close to the top corners while the smaller ones are on the unstable side, below the bottom corner bisectors. In the range of $0.6\leqslant Ro_\tau\leqslant 1.2$, these small secondary cells, near the bottom wall, increase their size as the rotational number is increased [see Figs. 4(c) and 4(e)] and recirculate part of the descending current towards the bottom wall bisector. At the highest rotation rate considered ($Ro_\tau=1.5$), the large and small cells are stretched to the lateral walls and to the bottom wall, respectively. The mean streamwise velocity contours in this case [Fig. 4(f)] reveal a fairly wide region ($0.35<z<0.65$) in the central part of the duct where $\partial U/\partial z\approx 0$, indicating the existence of a Taylor–Proudman regime. The sequence of cross-stream flows, in the range of $Ro_\tau>0.6$ as the rotation rate is increased, agrees qualitatively with the experimental observations of Hart[11] and simulations by Speziale[12] in the laminar regime.

B. Momentum budgets

Analysis of the mechanisms that affect the streamwise velocity distributions was made examining the terms of the resolved dimensionless Reynolds averaged x-momentum equation which, for a fully developed flow, reads as

Downloaded 19 Sep 2001 to 129.16.64.43. Redistribution subject to AIP license or copyright, see http://ojps.aip.org/phf/phfcr.jsp

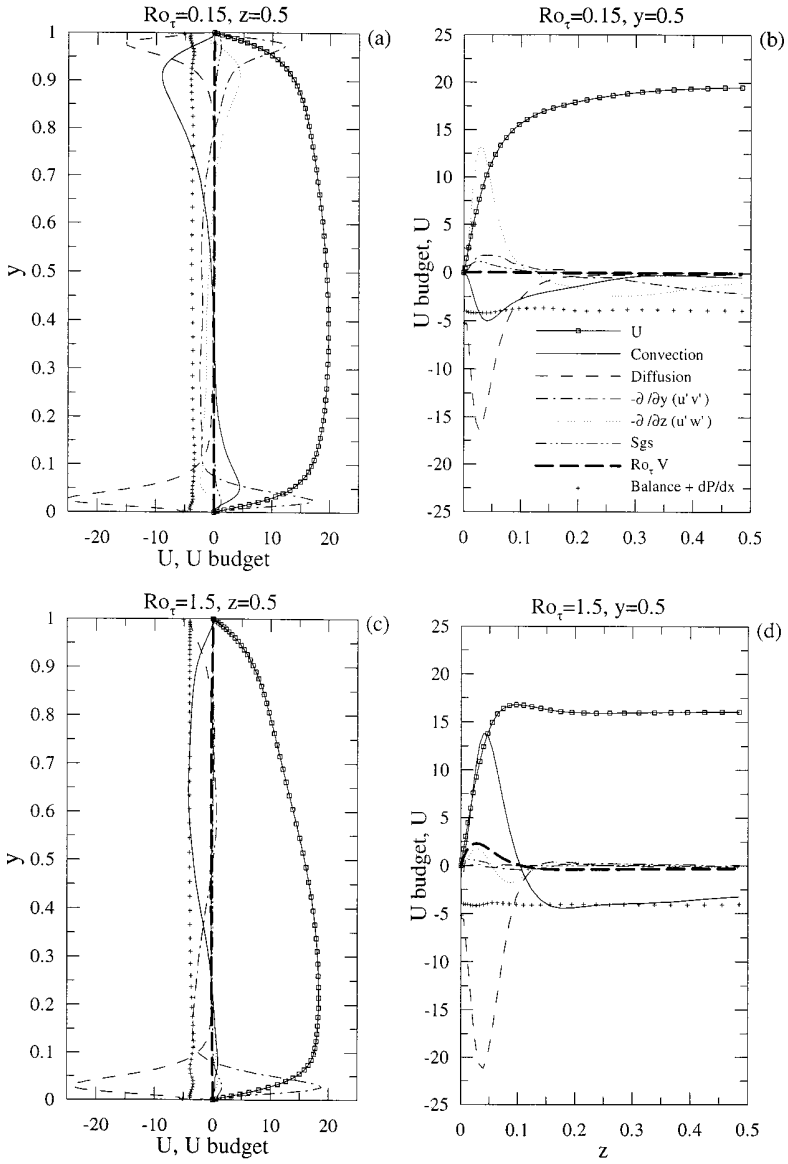

FIG. 5. Calculated x-momentum budget along the vertical and horizontal wall bisectors at $\mathrm{Ro}_\tau=0.15$ and $\mathrm{Ro}_\tau=1.5$.

$$-\left(V\frac{\partial U}{\partial y}+W\frac{\partial U}{\partial z}\right)-\left(\frac{\partial\langle u'v'\rangle}{\partial y}+\frac{\partial\langle u'w'\rangle}{\partial z}\right)+\frac{1}{\mathrm{Re}_\tau}\left(\frac{\partial^2}{\partial y^2}+\frac{\partial^2}{\partial z^2}\right)U+\mathrm{Ro}_\tau V+\mathrm{SGS}_U=-4. \tag{9}$$

The terms on the left hand-side of Eq. (9) are responsible, from left to right, for convection, turbulent transport, viscous diffusion, Coriolis effects and SGS transport, respectively.

The right-hand side corresponds to the nondimensional driving pressure gradient, dP/dx. The terms in the U equation along the wall bisectors at $\mathrm{Ro}_\tau=0.15$ and $\mathrm{Ro}_\tau=1.5$ are plotted in Fig. 5 as they appear in Eq. (9). The corresponding streamwise velocity profiles have also been included in this figure. It can be seen that the SGS transport term makes no significant contribution to the average x-momentum budgets shown in Fig. 5.

The spatial distributions of the different terms in Figs. 5(a) and 5(b) ($\mathrm{Ro}_\tau=0.15$) are qualitatively the same as reported by Huser and Biringen[10] at the wall bisector for the nonrotating turbulent duct flow. Figures 5(a) and 5(b) show that the x-component of the Coriolis force ($\mathrm{Ro}_\tau V$) makes no significant contribution to the U-momentum balance because of the low rotation number. At $\mathrm{Ro}_\tau=0.15$, the sum of the primary Reynolds shear stress gradients balances the imposed streamwise pressure gradient in the central region of the duct [Figs. 5(a) and 5(b)]. Close to the top [Fig. 5(a)] and side walls [Fig. 5(b)], diffusive and convective effects contribute to the loss of momentum while the sum of the Reynolds stresses terms acts as a source in Eq. (9), favoring the transport of high momentum fluid in the central part of the duct to the walls. The contribution of the convective term on the stable side, near the top wall [Fig. 5(a)], is larger than the one on the unstable side due to the intensification of the Coriolis-generated central descending current [see Fig. 4(a)].

At $\mathrm{Ro}_\tau=1.5$ the turbulent transport is completely suppressed on the stable side, and the main contribution of these terms is restricted to the region close to the bottom wall, on the unstable side [Fig. 5(c)]. Figures 5(c), 5(d) and 4(f) show

Downloaded 19 Sep 2001 to 129.16.64.43. Redistribution subject to AIP license or copyright, see http://ojps.aip.org/phf/phfcr.jsp

that at $\mathrm{Ro}_\tau = 1.5$, vertical convection ($V\partial U/\partial y$), which is about one order of magnitude larger than $W\partial U/\partial z$, is the most important contribution to balance the pressure gradient in the central part of the duct.

Note that, in the central part of the rotating channel [see Fig. 2(c)], the imposed pressure gradient is balanced by the turbulent transport term, $d\langle u'v'\rangle/dy$ [Eq. (9)]. As shown in Fig. 2(c), the effect of positive rotation in channel flow produces a region of a quasi-linear U profile with positive constant slope ($dU/dy > 0$) and a displacement of the maximum of U towards the top (stable) wall.

As the positive rotation rate is increased in the square duct, the augmentation of the vertical descending convective transport in the central region of the duct caused by the vertical Coriolis force component imposes a negative value of the main strain component ($\partial U/\partial y < 0$), consequently displacing the maximum of U towards the bottom (unstable) wall (see Fig. 4). In the range $\mathrm{Ro}_\tau \leqslant 1.2$ vertical profiles of the streamwise velocity do not exhibit a linear behavior in the central part of the duct. However, the profile of U shown in Fig. 5(c) ($\mathrm{Ro}_\tau = 1.5$) has a fairly constant slope of about $-20 \pm 2u_\tau/D$ in the range $0.5 < y < 0.8$. The region of quasi-linear velocity profile corresponds to a dominance of the vertical convection of momentum in the U budget. This dominance makes it reasonable to rewrite Eq. (9) as $-V dU/dy \approx -4$. In this central region, at $\mathrm{Ro}_\tau = 1.5$, the averaged vertical velocities are approximately constant, $V \approx -0.2u_\tau$ [see Fig. 4(f)]. The above simplified momentum equation explains the relatively high negative vertical gradient in the vertical streamwise velocity profile of Fig. 5(c) in the range of $0.5 \leqslant y \leqslant 0.8$. This suggests that the proper scale for the local main shear vorticity in the central part of the duct should be a mean velocity. Indeed, at $\mathrm{Ro}_\tau = 1.5$, if the parameter $S (S = -\mathrm{Ro}_\tau/dU/dy)$ is scaled by the mean velocity in the vertical symmetry midplane ($U_o/u_\tau = 13.4$), the balance between the background vorticity and the local main shear vorticity is recovered, $(-\mathrm{Ro}_\tau/dU/dy)\,(U_o/u_\tau) \approx 1$. In this case, $S > 0$ and thus the region of approximately constant dU/dy is on the stable side.

At $\mathrm{Ro}_\tau = 1.5$ [Fig. 5(d)] and near the lateral wall ($z < 0.1$), the loss of momentum produced by the diffusive term is balanced primarily by the relatively high convection caused by the vertical velocity. For example, at $z = 0.04$, $V\partial U/\partial y$ is about ten times larger than $W\partial U/\partial z$. As expected, the contribution of the Coriolis term is increased, compared with the one at $\mathrm{Ro}_\tau = 0.15$ [Fig. 5(b)]. However, the maximum of the Coriolis term in Fig. 5(d) is only about 15% of the dominant vertical convection.

It can be seen in Fig. 5(d) that the vertical convection of x-momentum from the stable side to the unstable side across the central part of the duct, combined with the convection in the opposite sense occurring near the lateral walls, explains the displacement of the maximum of the axial velocity, as the rotation rate is increased from the center of the duct towards the side walls. Figure 5(d) shows that the position of the local maximum of U ($z = 0.1$) at $\mathrm{Ro}_\tau = 1.5$ occurs where the dominant vertical convective transport is weak. It can be seen in Fig. 4(f) ($\mathrm{Ro}_\tau = 1.5$) that the distortion towards the top wall ($y = 1$) of the streamwise velocity contours near the side walls is produced where the vertical convection, $V\partial U/\partial y$, is reduced by the presence of the centers of the large stretched secondary cells. The absolute maximum of U is located in the symmetry midplane ($z = 0.5$) at low rotation rates ($\mathrm{Ro}_\tau = 0.15$ and $\mathrm{Ro}_\tau = 0.30$). In the range of $0.6 \leqslant \mathrm{Ro}_\tau \leqslant 1.5$, the U fields have two maxima symmetrically distributed with respect to the vertical midplane. These maxima are shifted towards the bottom and lateral walls as the rotation rate is increased. For example, the position of the maximum at $\mathrm{Ro}_\tau = 0.3$ is $y = 0.30$, $z = 0.50$; at $\mathrm{Ro}_\tau = 0.9$, $y = 0.21$, $z = 0.12$ and at $\mathrm{Ro}_\tau = 1.2$, $y = 0.14$, $z = 0.11$. Note that, by definition, the convective transport is zero at the position of the absolute maximum ($\partial U/\partial y = 0$ and $\partial U/\partial z = 0$). This indicates that the displacement of the maxima towards the side walls is produced by the formation of the large cells near the side walls which progressively increase the vertical cross-stream convective motion from the stable side, across the central part of the duct, towards the bottom corners.

C. Turbulence intensities' spatial distributions

Figures 6 and 7 show the cross-stream spatial distributions of the averaged normal and shear Reynolds stresses at $\mathrm{Ro}_\tau = 0$, 0.15 and $\mathrm{Ro}_\tau = 0.9$, 1.5, respectively. Intensities shown in these figures have been scaled with the bulk velocity,

$$\langle u_i' u_j' \rangle^* = 100 \langle u_i' u_j' \rangle / U_b^2.$$

This scaling has been chosen to take into account the variability of the mean flow at different values of Ro_τ. Contours of the turbulence intensities at $\mathrm{Ro}_\tau = 0$ and $\mathrm{Ro}_\tau = 0.9$ (continuous lines) are plotted together with the ones corresponding to $\mathrm{Ro}_\tau = 0.15$ and $\mathrm{Ro}_\tau = 1.5$ (discontinuous lines).

Rotation effects on the Reynolds stresses components in a rotating channel flow can be analyzed by examining the generation terms (M_{ij}) in the turbulent stresses transport equations.[1,5,25] Generation terms are associated with mean shear (P_{ij}) and rotational stress production (G_{ij}). These terms appear in Eq. (10) scaled with the bulk velocity,

$$\begin{aligned} M_{ij} &= P_{ij} + G_{ij}, \\ P_{ij}^* &= -\left[\langle u_i' u_k' \rangle^* \frac{\partial U_j^*}{\partial x_k} + \langle u_j' u_k' \rangle^* \frac{\partial U_i^*}{\partial x_k} \right], \\ G_{ij}^* &= -\frac{2\Omega_k D}{U_b} [\langle u_j' u_m' \rangle^* \in_{ikm} + \langle u_i' u_m' \rangle^* \in_{jkm}]. \end{aligned} \tag{10}$$

To facilitate the interpretation of the following discussion, the different terms of P_{ij}^* and G_{ij}^* can be found in the Appendix for a fully developed rotating duct flow. The dominant terms in the different components of P_{ij}^* and G_{ij}^* for the flow conditions simulated appear underlined in the Appendix. Figure 8 shows a sketch of the main relations between the normal and main shear stresses for the present simulations. It should be noted that Fig. 8 represents a simplified picture of the complex relationships between the Reynolds stress components through the generation terms.

The computation of the spatial distributions of the resolved part of the generation rates for each Reynolds stress

Downloaded 19 Sep 2001 to 129.16.64.43. Redistribution subject to AIP license or copyright, see http://ojps.aip.org/phf/phfcr.jsp

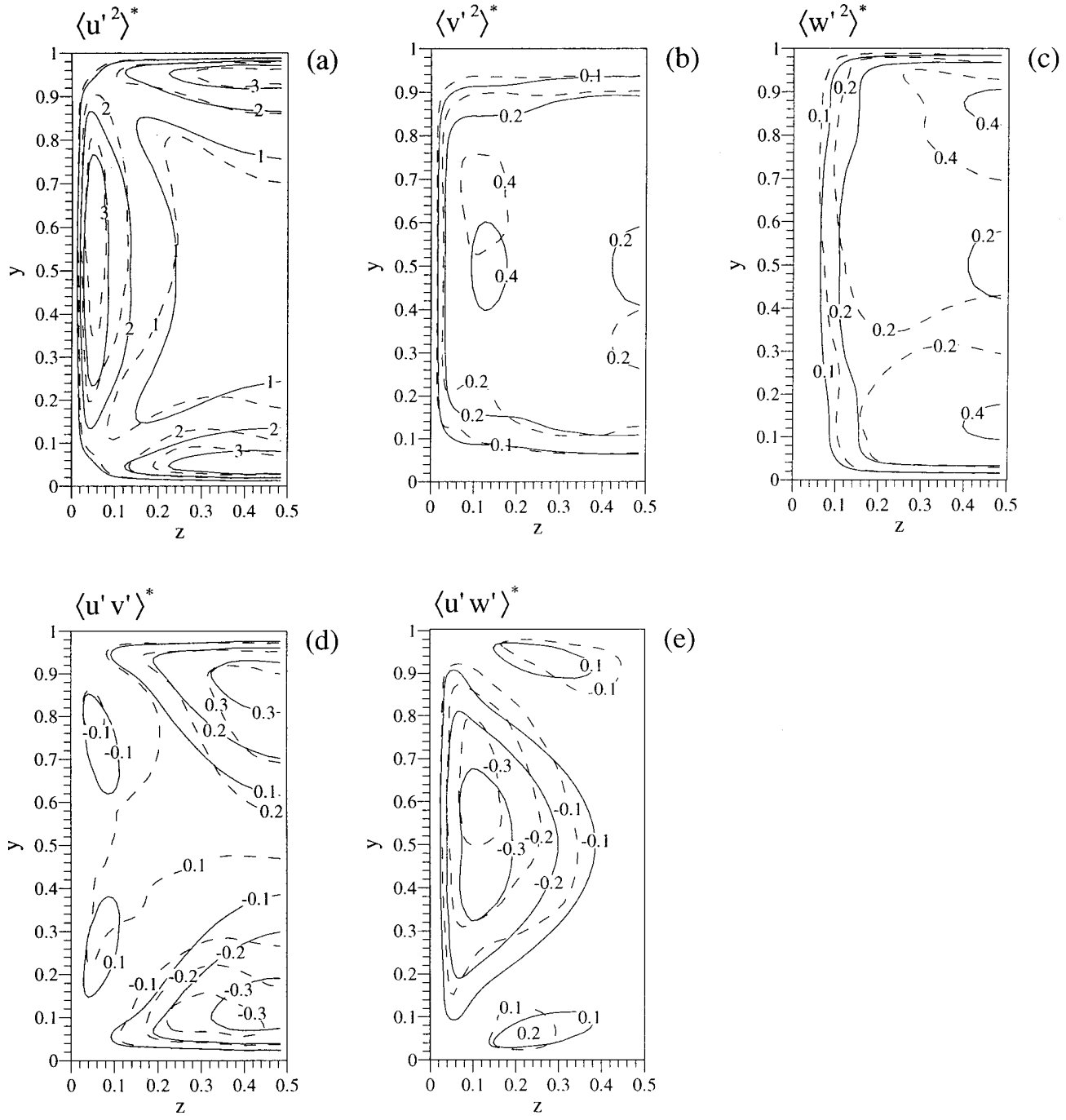

FIG. 6. Spatial distributions of the resolved Reynolds stress components in square duct flow at $\mathrm{Re}_\tau=300$. (a) $\langle u'^2\rangle^*$, (b) $\langle v'^2\rangle^*$, (c) $\langle w'^2\rangle^*$, (d) $\langle u'v'\rangle^*$ and (e) $\langle u'w'\rangle^*$ at $\mathrm{Ro}_\tau=0$ (continuous lines) and $\mathrm{Ro}_\tau=0.15$ (discontinuous lines).

component in the range of Ro_τ covered revealed that regions of high/low M_{ij} lead to high/low values in the $\langle u'^2\rangle^*$, $\langle u'v'\rangle^*$ and $\langle u'w'\rangle^*$ components owing to the contribution of the main shear ($\partial U/\partial y, \partial U/\partial z$) in the corresponding production terms, P_{11}^*, P_{12}^* and P_{13}^* (see Fig. 8). The contributions of the terms that contain secondary strains ($\partial V/\partial x_j, \partial W/\partial x_j$) or the secondary shear stress, $\langle v'w'\rangle^*$, in P_{12}^* and P_{13}^*, are about an order of magnitude smaller than those of the terms containing products of main strains ($\partial U/\partial y, \partial U/\partial z$) and normal stresses. On the other hand, distributions of the generation rates, P_{22}^*, P_{33}^* and P_{23}^*, which contain only secondary strains ($\partial V/\partial y$, $\partial V/\partial z$ and $\partial W/\partial y$), were not directly related to the corresponding Reynolds stresses distributions ($\langle v'^2\rangle^*$, $\langle w'^2\rangle^*$ and $\langle v'w'\rangle^*$). In fact, regions where these stresses attain their extreme values correspond to regions where the generation rates are very weak. This supports the idea that, as in channel flow ($P_{22}^*=P_{33}^*=P_{23}^*=0$), the distributions of $\langle v'^2\rangle^*$ and $\langle w'^2\rangle^*$ are more influenced by the velocity pressure–gradient terms.[26] The velocity pressure–gradient terms (Π_{ij}) are usually split into a

Downloaded 19 Sep 2001 to 129.16.64.43. Redistribution subject to AIP license or copyright, see http://ojps.aip.org/phf/phfcr.jsp

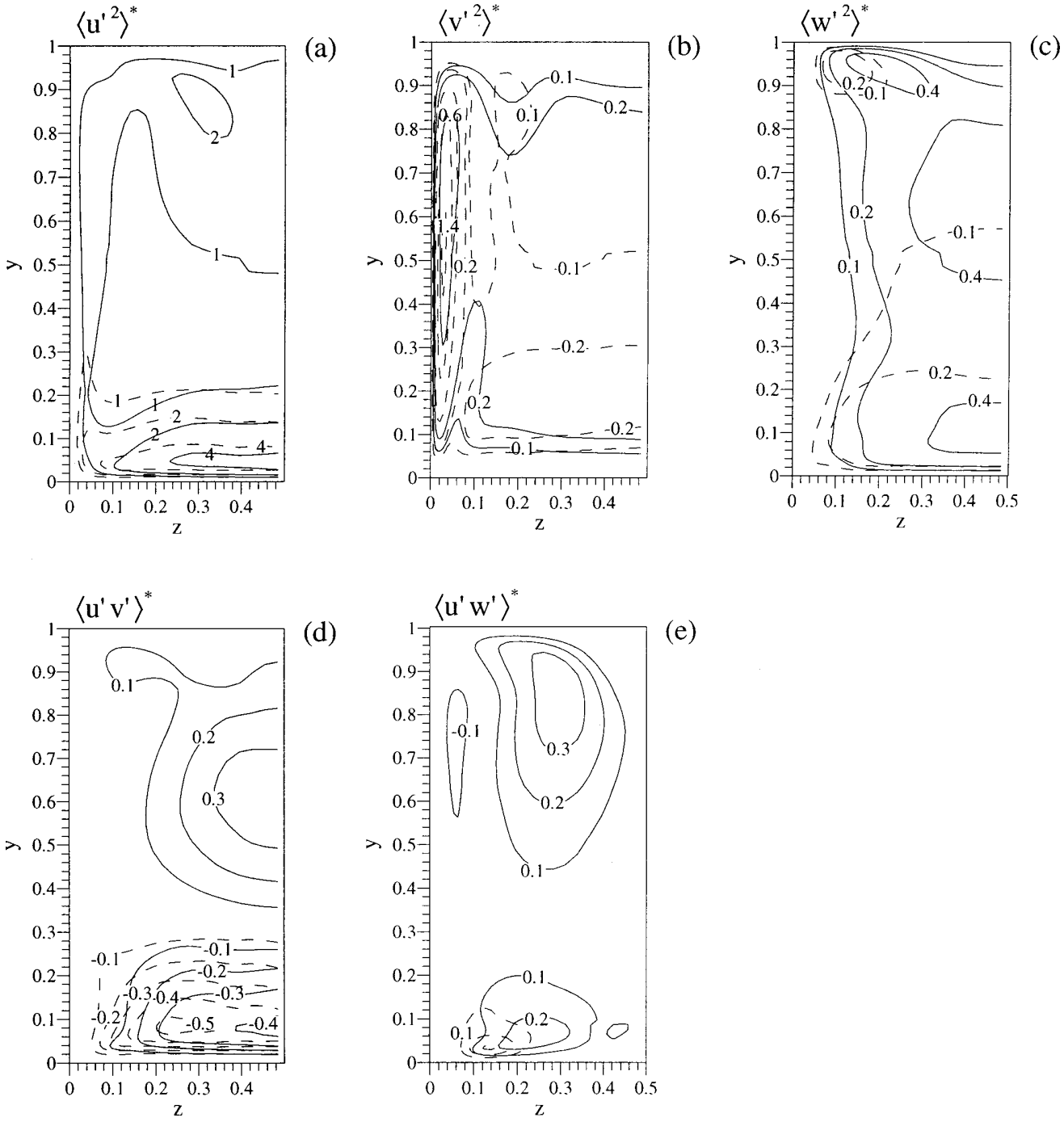

FIG. 7. Spatial distributions of the resolved Reynolds stress components in rotating square duct flow at $\mathrm{Re}_\tau=300$. (a) $\langle u'^2\rangle^*$, (b) $\langle v'^2\rangle^*$, (c) $\langle w'^2\rangle^*$, (d) $\langle u'v'\rangle^*$, and (e) $\langle u'w'\rangle^*$ at $\mathrm{Ro}_\tau=0.9$ (continuous lines) and $\mathrm{Ro}_\tau=1.5$ (discontinuous lines).

pressure–transport term and a redistributive traceless term (ϕ_{ij}), known as the pressure–strain term. As shown in Mansour *et al.*[26] in an analysis of DNS data of fully developed turbulent channel flow, ϕ_{ij} is the most important contribution to Π_{ij} in the buffer and log layers. The role of the pressure–strain interaction in the transport equations for the normal turbulent stresses is associated with a redistribution of turbulent energy among the normal stresses, transferring energy from the component that receives most of the production by mean shear, $\langle u'^2\rangle^*$, to the other normal components, $\langle v'^2\rangle^*$ and $\langle w'^2\rangle^*$. Computations of the distributions of the resolved velocity pressure-gradient terms in the rotating square duct flow at the highest rotational number considered show that there is a correspondence between regions where Π_{22} and Π_{33} have local maxima and regions where the distributions of $\langle v'^2\rangle^*$ and $\langle w'^2\rangle^*$ attain high values, indicating energy transfer among the normal stresses.

At low rotation rates ($\mathrm{Ro}_\tau=0.15$ and $\mathrm{Ro}_\tau=0.3$), the con-

Downloaded 19 Sep 2001 to 129.16.64.43. Redistribution subject to AIP license or copyright, see http://ojps.aip.org/phf/phfcr.jsp

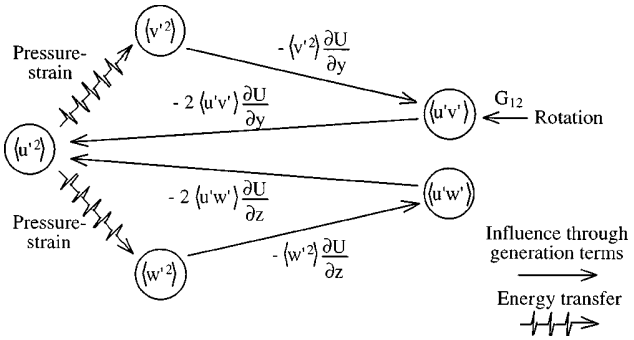

FIG. 8. Main pressure-strain energy transfer processes and main relationships between the Reynolds stresses components through the generation terms M_{ij}.

tribution of G_{ij}^* to the overall generation rate (M_{ij}^*) is small compared with that of P_{ij}^*. Computations of the distributions of the rotation shear tensor components show that, at higher rotation rates, G_{12}^* is the dominant component of G_{ij}^* with a contribution to M_{12}^* of the same order as that of P_{12}^*.

It can be seen in Figs. 6 and 7 that, in general, as the rotation rate is increased, the main effect of rotation is to increase/reduce $\langle u'^2\rangle^*$ on the unstable/stable side and to redistribute the regions of high values of $\langle v'^2\rangle^*$ and $\langle w'^2\rangle^*$. The normal stresses, $\langle v'^2\rangle^*$ [Figs. 6(b) and 7(b)] and $\langle w'^2\rangle^*$ [Figs. 6(c) and 7(c)], attain their maxima near the side walls and near the horizontal walls, respectively, where high values of the corresponding velocity pressure–gradient terms occur. Note that, for example, the energy transfer from $\langle u'^2\rangle^*$ to $\langle w'^2\rangle^*$ near the side wall $z=0$ is inhibited by the damping effect of the wall. Figure 7(b) shows that, at $\mathrm{Ro}_\tau=0.9$ and $\mathrm{Ro}_\tau=1.5$, the fields of $\langle v'^2\rangle^*$ have marked maxima near the lateral walls where the Coriolis-generated ascending currents occur [see Figs. 4(d) and 4(f)]. Correspondingly, the distributions of $\langle w'^2\rangle^*$ at $\mathrm{Ro}_\tau=0.9$ and $\mathrm{Ro}_\tau=1.5$ [Fig. 7(c)] have local maxima near the top wall, where the secondary flows convect the ascending currents towards the top wall bisector [see Figs. 4(d) and 4(f)].

Figures 6(e) and 7(e) show that the negative extreme values of $\langle u'w'\rangle^*$ near the side wall $z=0$ present at $\mathrm{Ro}_\tau=0.15$ are considerably reduced at $\mathrm{Ro}_\tau=0.9$ according to the reduction of $\langle w'^2\rangle^*$, and thus of P_{13}^*, in this region [see Fig. 7(c)]. At $\mathrm{Ro}_\tau=0.9$, there is a noticeable increase in positive values of $\langle u'w'\rangle^*$ near $y=0.8$, $z=0.25$ in accordance with the displacement of the contours of $\langle w'^2\rangle^*$ [see Fig. 7(c)] and the augmentation of $-\partial U^*/\partial z$ [see Fig. 4(d)]. At $\mathrm{Ro}_\tau=1.5$, $\langle u'w'\rangle^*$ [Fig. 7(e)] is suppressed because of the stabilization of the flow ($\partial U^*/\partial z\approx 0$, in the central part of the duct) and the reduction of $\langle w'^2\rangle^*$.

Figure 8 shows that the distributions of $\langle u'v'\rangle^*$ are mainly affected by the term $-\langle v'^2\rangle^*\partial U^*/\partial y$ in P_{12}^* and, at high rotation rates, by G_{12}^*. It should be noted that regions where $\langle u'v'\rangle^*$ is positive/negative correspond to regions where $\partial U/\partial y$ is negative/positive. Figures 6(d) and 7(d) show that, at $\mathrm{Ro}_\tau=0.9$, the positive maximum of $\langle u'v'\rangle^*$ on the stable side is displaced towards the horizontal midplane $y=0.5$ according to the changes in the distributions of $\langle v'^2\rangle^*$ in this region [Figs. 7(b)]. The positive maximum present at $\mathrm{Ro}_\tau=0.9$ is suppressed at $\mathrm{Ro}_\tau=1.5$ which corresponds to a reduction of $\langle v'^2\rangle^*$, and of P_{12}^*, in the central region of the duct [Fig. 7(b)]. For example, at $\mathrm{Ro}_\tau=0.9$ and $y=0.6$, $z=0.45$, $P_{12}^*=0.41$ and $G_{12}^*=-0.061$ while in the same location at $\mathrm{Ro}_\tau=1.5$, $P_{12}^*=0.063$ and $G_{12}^*=-0.040$. At $\mathrm{Ro}_\tau=1.5$, large negative values of $\langle u'v'\rangle^*$ near the bottom wall are influenced and maintained by the rotation and main shear terms. As an example, at $\mathrm{Ro}_\tau=0.9$ and $y=0.1$, $z=0.45$, $P_{12}^*=-0.57$ and $G_{12}^*=-0.17$, while at $\mathrm{Ro}_\tau=1.5$, in the same location, $P_{12}^*=-0.33$ and $G_{12}^*=-0.33$

The volume averaged turbulent kinetic energy, $\langle K\rangle_V^*$, scaled with the bulk velocity, has been plotted as a function of Ro in Fig. 9. It can be seen in Fig. 9 that most of the reduction of the turbulent kinetic energy is produced by a progressive decrease in the energy level of the streamwise Reynolds stress component which receives energy from the main shear. The contributions of $\langle v'^2\rangle^*$ and $\langle w'^2\rangle^*$ to $\langle K\rangle_V^*$ remain fairly constant in the range of $\mathrm{Ro}\leqslant 0.087$ ($\mathrm{Ro}_\tau\leqslant 1.2$). When the rotation rate is increased from $\mathrm{Ro}_\tau=1.2$ to $\mathrm{Ro}_\tau=1.5$ there is a reduction, by about 34%, of $\langle K\rangle_V^*$. This important reduction corresponds, as described before, to the development of a Taylor–Proudman regime in the central part of the duct ($\partial U/\partial z\approx 0$) which reduces the term $-2\langle u'w'\rangle^*\partial U^*/\partial z$ in P_{11}^*. The remaining term in P_{11}^*, $-2\langle u'v'\rangle^*\partial U^*/\partial y$, is also reduced at high rotation rates because of the complete suppression of $\langle u'v'\rangle^*$ on the stable side by the effect of G_{12}^*.

It can be seen, from Fig. 9 and from the previous discussion of Figs. 6 and 7 that, in general, the main effect of rotation on the square duct flow is a stabilizing one i.e., a global reduction of the turbulence intensities. Consequently, a decrease in the turbulent mixing of any passive scalar present in the flow is expected as the rotation rate is increased.

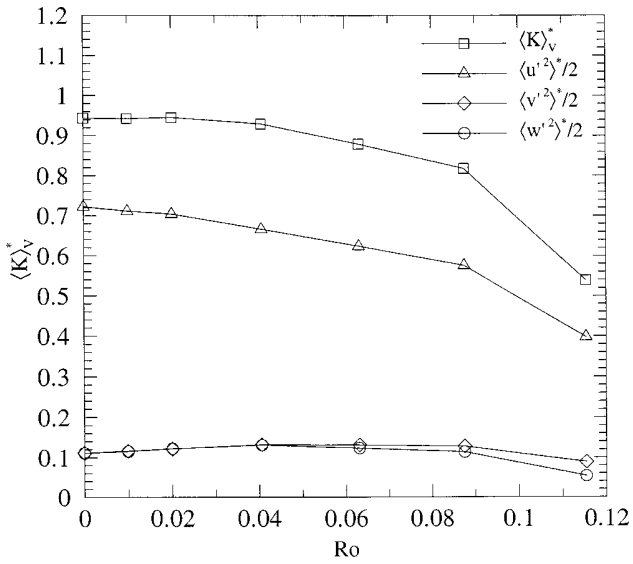

FIG. 9. Volume averaged turbulent kinetic energy and its contributions as a function of Ro.

Downloaded 19 Sep 2001 to 129.16.64.43. Redistribution subject to AIP license or copyright, see http://ojps.aip.org/phf/phfcr.jsp

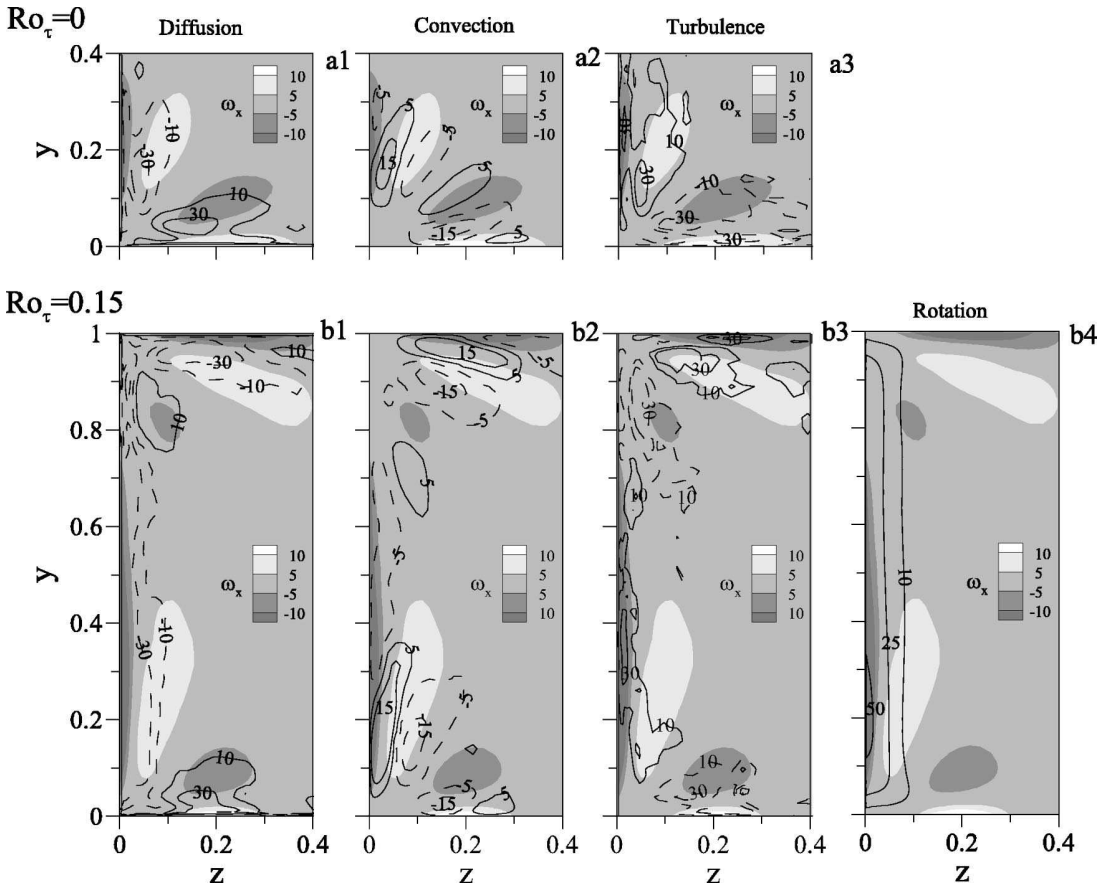

FIG. 10. Distributions of the resolved mean streamwise vorticity and the terms of the governing transport equation at $\mathrm{Ro}_\tau=0$ (a) and at $\mathrm{Ro}_\tau=0.15$ (b). Continuous line contours correspond to positive values, while negative contours have been plotted with dashed lines.

D. Wall friction velocities

Mean wall friction velocities at the unstable (bottom) and stable (top) walls of the rotating square duct flow in the range of rotational numbers considered are shown in Fig. 3. It can be seen that present duct flow predictions reproduce the levelling off of the u_τ on the unstable side at $\mathrm{Ro}>0.05$ in agreement with DNS rotating channel data. The rapid decrease of the wall friction velocity at the stable wall, not observed in simulations of rotating channel flow at high rotational numbers[5] corresponds, as discussed in the previous subsection, to the progressive suppression of the turbulence intensities on the stable side as the rotational number is increased. As shown in Fig. 3, this tendency agrees with the low Reynolds numbers experiments of Johnston *et al.*[1] in a rotating rectangular duct of aspect ratio 7.1. This supports the idea that the transition from turbulent to laminar flow on the stable side of a finite aspect ratio rectangular the duct is produced by the development of a persistent stabilizing convective momentum transfer in the central part of the duct.

E. Mean streamwise vorticity equation

The formation of secondary flows in nonrotating ducts has been studied in numerical work[8–10] analyzing the terms of the mean streamwise vorticity transport equation [Eq. (11)]. This equation for a fully developed flow in a rotating frame of reference with the axis of rotation parallel to the z direction reads as

$$\left(\frac{\partial}{\partial z}\left\{\left(\frac{1}{\mathrm{Re}_\tau}+\nu_T\right)\frac{\partial}{\partial z}\right\}+\frac{\partial}{\partial y}\left\{\left(\frac{1}{\mathrm{Re}_\tau}+\nu_T\right)\frac{\partial}{\partial y}\right\}\right)\omega_x - \left(V\frac{\partial}{\partial y}+W\frac{\partial}{\partial z}\right)\omega_x+\left(\frac{\partial^2}{\partial y\,\partial z}(\langle v'^2\rangle-\langle w'^2\rangle)\right) + \left(\frac{\partial^2}{\partial z^2}-\frac{\partial^2}{\partial y^2}\right)\langle v'w'\rangle+\mathrm{Ro}_\tau\frac{\partial U}{\partial z}+\mathrm{SGS}_{\omega_x}=0, \tag{11}$$

where ω_x is the resolved mean streamwise vorticity ($\omega_x=\partial W/\partial y-\partial V/\partial z$). The last term in Eq. (11) is a relatively complicated expression involving ν_T. This term equals zero if ν_T were a constant. It has been evaluated and found negligibly small compared with the dominant terms in Eq. (11).

Figures 10 and 11 show the averaged spatial distributions of the first five terms of Eq. (11) at $\mathrm{Ro}_\tau=0$, 0.15, 0.9 and 1.5. The two-dimensional fields of the different terms of Eq. (11) are superimposed to filled contours of the mean streamwise vorticity. Light/dark gray regions indicate positive/negative values of ω_x. Fields in $z>0.6$, not shown in Figs. 10 and 11, are antisymmetric with respect to $z=0.5$ to those plotted in these figures.

Downloaded 19 Sep 2001 to 129.16.64.43. Redistribution subject to AIP license or copyright, see http://ojps.aip.org/phf/phfcr.jsp

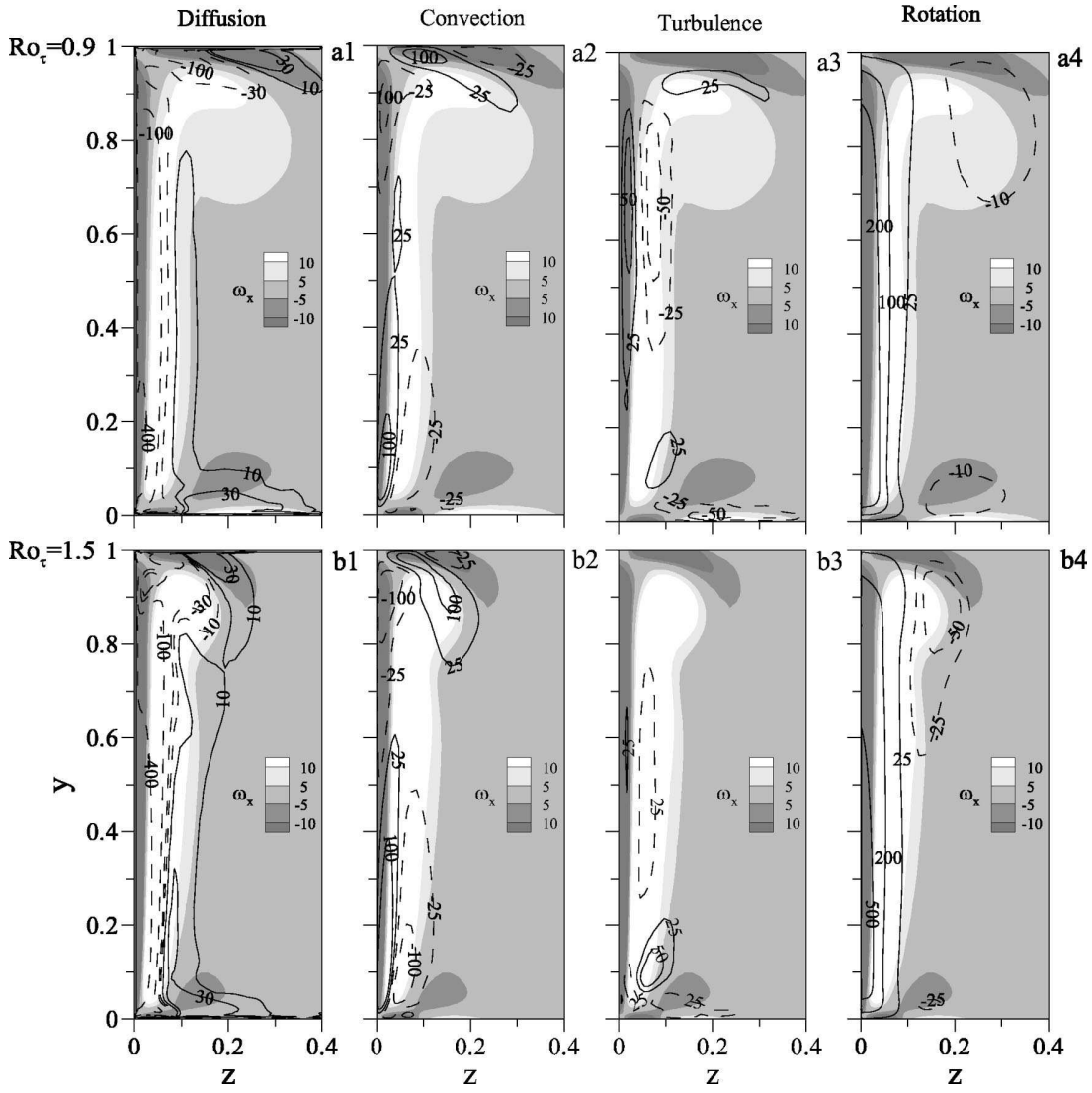

FIG. 11. Distributions of the resolved mean streamwise vorticity and the terms of the governing transport equation at $\mathrm{Ro}_\tau = 0.9$ (a) and at $\mathrm{Ro}_\tau = 1.5$. (b). Continuous line contours correspond to positive values, while negative contours have been plotted with dashed lines.

The first two terms of Eq. (11), at $\mathrm{Ro}_\tau = 0$, depicted in Figs. 10(a1) and 10(a2), are responsible for the diffusion and convection of ω_x, respectively. It can be seen in Fig. 10(a1) that ω_x has positive/negative extreme values at the horizontal/vertical walls. In the center of the cells, ω_x attains local extreme values which are about 47% of the absolute maximum and minimum values located at the horizontal and vertical walls, because of the nonslip condition for velocities. The role of the diffusive term has been described in Gavrilakis[9] and Huser and Biringen[10] and, as shown in Fig. 10(a1), it contributes, in Eq. (11), as a source along the viscous sub-layers, but as a sink in the core of the secondary flows. The convective term represents the smallest contribution to Eq. (11) when $\mathrm{Ro}_\tau = 0$. Figure 10(a2) shows that it acts as a transport term with a high contribution to the ω_x budget between regions where extreme values of vorticity occur, i.e., near the walls and in the centers of the cells. Note also that convection attains high values between the cells and the corner bisector where the streamwise vorticity vanishes. The sum of the third and fourth terms, which is the main contribution of turbulence to Eq. (11), has been plotted in Fig. 10(a3). It can be seen that this term acts as a transport term between extreme values of ω_x and it represents the main contribution to the production of vorticity in the core of the cells. General agreement is found when comparing the spatial distributions of the terms of Eq. (11) in Figs. 10(a) with the ones in Gavrilakis[9] at the same Reynolds number in his Fig. 17.

The fifth term on the left-hand side of Eq. (11) is the influence of the Coriolis force and is responsible of the loss of antisymmetry, with respect to the plane $y = 0.5$, of the mean streamwise vorticity field when rotation is considered. Equation (11) indicates that, at rotation rates high enough to suppress the turbulence intensities on the stable side and in regions of constant ω_x, the axial velocity component should not change in the direction of the rotation vector, i.e., the Taylor–Proudman regime. As shown in Fig. 4(f) and discussed in Sec. IV A, this flow develops at $\mathrm{Ro}_\tau = 1.5$, in the

Downloaded 19 Sep 2001 to 129.16.64.43. Redistribution subject to AIP license or copyright, see http://ojps.aip.org/phf/phfcr.jsp

central region of the duct where the imposed pressure gradient is balanced primarily by the vertical convection of U [see Fig. 5(c)].

At $\mathrm{Ro}_\tau=0.15$ the rotational term [Fig. 10(b4)] acts, in Eq. (11), as a source of positive ω_x near the side wall $z=0$. It is the main contributor to the amplification/reduction, as the rotation rate is increased from $\mathrm{Ro}_\tau=0$ to $\mathrm{Ro}_\tau=0.15$, of the cell with positive/negative ω_x close to the side wall $z=0$. Note that the contribution of the turbulence term does not change significantly as the rotation rate is increased from $\mathrm{Ro}_\tau=0$ to $\mathrm{Ro}_\tau=0.15$, in the reduced cell with negative ω_x of the top left quadrant. The local maximum of ω_x at the center of the bottom/top cell close to $z=0$ is increased/decreased by about 15%/23%. As expected, the diffusive term [Fig. 10(b1)] tends to balance part of the effect of the rotational [Fig. 10(b4)] and turbulence [Fig. 10(b3)] terms near the side wall $z=0$, as can be seen comparing Figs. 10(a1) ($\mathrm{Ro}_\tau=0$) and 10(b1) ($\mathrm{Ro}_\tau=0.15$). As the rotation rate is increased, there is a noticeably increasing contribution of the terms responsible for the convective transport of ω_x from and to the large secondary flows with positive ω_x in the bottom and top quadrants [Figs. 10(a2) and 10(b2)] in accordance with the intensification of the cross-stream recirculating flow rate.

Figures 11(a) and 11(b) show the spatial distributions of the different terms of Eq. (11) at $\mathrm{Ro}_\tau=0.9$ and $\mathrm{Ro}_\tau=1.5$, respectively. It can be seen that the streamwise vorticity near the side walls is dominated mainly by the diffusive [Figs. 11(a1) and 11(b1)] and rotational [Figs. 11(a4) and 11(b4)] terms with an important intensification, as compared with the low rotation rate case, of the convective terms [Figs. 11(a2) and 11(b2)] because of the increase in cross-stream velocities components and of ω_x. At $\mathrm{Ro}_\tau=0.9$ and $\mathrm{Ro}_\tau=1.5$, the turbulence term acts as a source of positive vorticity, where $\omega_x<0$ with a contribution of about 20% as compared with the rotational term and to a sink of positive vorticity where $\omega_x>0$. Both terms, the anisotropy, with a contribution of 60%–80%, and secondary shear stress term, with a contribution of 40%–20%, are involved in the overall turbulence term near the side walls. Figure 11(a3) shows that the turbulence term is the main sink of positive vorticity near the bottom (unstable) wall, below the negative vorticity cell core. As discussed in Sec. IV B in the range of $0.6\leqslant \mathrm{Ro}_\tau \leqslant 1.2$, the small cells near the unstable (bottom) wall are progressively enlarged, as the rotational number is increased because high x-momentum fluid is displaced by the Coriolis-generated vertical convection towards the bottom corners on the unstable side and towards the side walls on the stable side. This generates a different behavior of the rotational term in the cores of the large and small secondary flows. As shown in Fig. 11(a4) ($\mathrm{Ro}_\tau=0.9$), the rotational term acts as a sink of positive vorticity ($\partial U/\partial z<0$) in part of the large secondary flow with positive streamwise vorticity and as a source of negative vorticity in the small secondary flow with negative streamwise vorticity. At $\mathrm{Ro}_\tau=0.9$, the contribution of the rotational term to the overall production of negative streamwise vorticity in the core of the small cell is about 50%. At $\mathrm{Ro}_\tau=1.2$, this contribution is increased up to 65%, which corresponds to the largest extension of these secondary flows observed in the range of rotational numbers studied. It can be seen from a comparison of Figs. 11(a) and 11(b) that the stretched topology of the core of the large secondary flow ($\omega_x>0$) at $\mathrm{Ro}_\tau=1.5$ corresponds to a significant increase in the production of negative streamwise vorticity by the rotational term.

F. Instantaneous flow visualizations

In this subsection we present some instantaneous flow fields to illustrate the effect of rotation on near-wall vortical flow structures. Instantaneous vortical structures were identified with the method developed by Jeong and Hussain.[27] These authors reviewed several methods for vortex identification and proposed a new definition based on the detection of local pressure minima caused by vortex cores. This definition establish that regions where the second largest eigenvalue of the tensor $S^2+\Omega^2$ has negative values correspond to the locations of the vortex cores. More details about this definition can be found elsewhere.[27]

Figure 12 shows instantaneous flow fields at $\mathrm{Ro}_\tau=0$, 0.9 and 1.5 using the definition proposed by Jeong and Hussain.[27] The resolved velocity flow field has been used to compute λ_2. The surfaces have been colored dark gray if $\omega_x>0$ and light gray if $\omega_x<0$ to show the sense of rotation of the streamwise vortices. The different views of the flow (front, top, right and left) are defined in Fig. 12. The opaque walls, $y=0.5$ and $z=0.5$, depicted in this figure hide the flow structures in $z>0.5$, $z<0.5$ and $y<0.5$ for the left, right and top views, respectively.

Figures 12(top-1) and 12(front-1) ($\mathrm{Ro}_\tau=0$) show the top and front view of the same instantaneous flow field. It can be seen in Fig. 12(top-1) that vortical structures with positive or negative streamwise vorticity near walls $z=0$ and $z=1$ tend to be inclined with respect to the x-direction, pointing towards the central part of the duct. The quasi-streamwise vortices near plane $z=0.5$ appear tilted in the x-z plane. Light/dark gray surfaces containing negative/positive streamwise vorticity tend to be tilted with a positive/negative angle. These orientations of the vortical structures agree qualitatively with those recently reported by Jeong *et al.*,[28] who used the λ_2 definition to educe near-wall coherent structures in turbulent channel flow. The front view [Fig. 12(front-1)] shows that most of the quasi-streamwise vortices plotted in Fig. 12(top-1) extend from the outer part of the viscous sublayer $y^+\approx 6$ to the log-layer $y^+\approx 70$. It is interesting to note the absence of surfaces and thus vortex cores in regions close to the corner bisectors. Inspection of the flow field in different cross-sections revealed that these regions correspond to a persistent momentum transfer from the central region of the duct towards the corners. As expected, vortical structures with positive/negative streamwise vorticity are about 60% more frequent in the octants where the secondary flows have positive/negative axial vorticity.

Figures 12(front-2) and 12(top-2) ($\mathrm{Ro}_\tau=0.9$) show the preponderance of vortex cores with negative/positive streamwise vorticity in the top right/left quadrant of the duct. Note that the streamwise vortices on the stable side tend to be twisted, following the swirling motions of the mean large secondary cells, shown in Fig. 4(d). Regions with a small

Downloaded 19 Sep 2001 to 129.16.64.43. Redistribution subject to AIP license or copyright, see http://ojps.aip.org/phf/phfcr.jsp

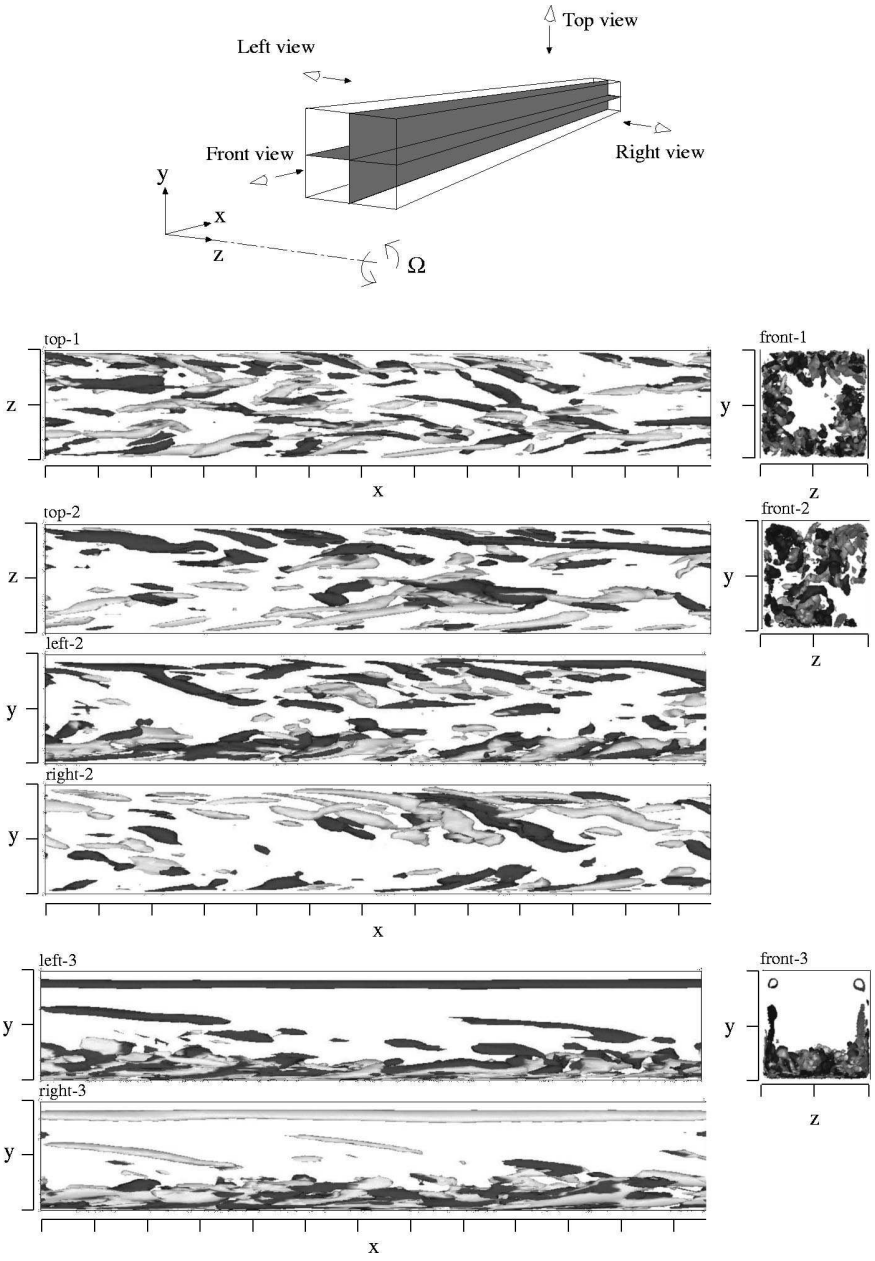

FIG. 12. Instantaneous flow visualizations in terms of surfaces of constant value of λ_2 colored with the instantaneous field of the streamwise vorticity. Dark gray if $\omega_x>0$ or light gray if $\omega_x<0$. Sketch of the different views of the flow. (top-1 and front-1) $\mathrm{Ro}_\tau=0$, $\lambda_2=-300$. (top-2, front-2, left-2 and right-2) $\mathrm{Ro}_\tau=0.9$, $\lambda_2=-300$. (front-3, left-3 and right-3) $\mathrm{Ro}_\tau=1.5$, $\lambda_2=-75$.

concentration of vortex cores, i.e., near the top wall bisector and near the bottom corner bisectors [Fig. 12(front-2)], correspond to persistent momentum transfer by the secondary flows. It can be seen in Figs. 12(left-2) and 12(right-2) that some streamwise vortices on the stable side have a considerably larger streamwise length than those on the unstable side.

Figure 12(front-3) ($\mathrm{Ro}_\tau=1.5$) shows a high concentration of streamwise vortices on the unstable side and a complete absence of vortex cores in the central part of the duct, where the Coriolis-generated descending vertical convection of momentum occurs [see Fig. 4(f)]. As discussed in Sec. IV B, this convective transport in the central part of the duct at $\mathrm{Ro}_\tau=1.5$ inhibits turbulent intensities (Fig. 7) and production of mean streamwise vorticity (Fig. 11). The existence of two counter-rotating persistent vortex tubes near the top corners of the duct (stable side) can be seen in Figs. 12(left-3) and 12(right-3). Several elongated wall vortices tend to drift from the unstable side to the stable side close and parallel to the side walls. Instantaneous velocity fields show that these streamwise vortices near the side walls are generated when high momentum fluid is convected towards the bottom corners. The impingement of this current produces an ejection of low momentum fluid from the bottom wall. On the side wall and near the bottom corner a streamwise vortex is generated. These vortices are inclined in the xy plane ($\omega_y<0$), as shown in Figs. 12(left-3) and 12(right-3). The inclination can be explained considering the term $\omega_j S_{ij}$ in the instantaneous vorticity transport equation. This term is responsible for the amplification, reduction or turning of the vorticity vector according to the dominant components of the strain rate tensor. It can be seen in Fig. 4(f) that the regions near

Downloaded 19 Sep 2001 to 129.16.64.43. Redistribution subject to AIP license or copyright, see http://ojps.aip.org/phf/phfcr.jsp

the side walls where these inclined vortex cores develop correspond to regions of persistent negative strain ($\partial U/\partial y<0$) which is produced by the existence of low x-momentum fluid near the top (stable) wall and high x-momentum fluid near the bottom (unstable) wall (see Fig. 4). This instantaneous flow structure at $\mathrm{Ro}_\tau=1.5$ is in agreement with the elongated mean secondary flows near the side walls shown in Fig. 4(f). Note that the instantaneous streamwise vortices on the stable side shown in Fig. 12(front-3) are sources of turbulence intensities near the side walls [Fig. 7(b)] and near the top corners [Fig. 7(c)].

V. CONCLUSIONS

Large-eddy simulations at low Reynolds numbers of stationary and rotating channel and square duct flows have been reported using the localized dynamical SGS model proposed by Kim and Menon.[14] The present results for nonrotating channel and duct flow, as well as simulations of rotating channel flow, are in good agreement with existing DNS data.

The effect of low rotation rates in the square duct flow produce substantial changes in the turbulence-driven secondary flows developed near the corners. The Coriolis-generated descending cross-stream current in the central part of the duct enhances the streamwise vorticity and the secondary flows, which convect this current upwards, near the side walls, and towards the central part of the duct. As in channel flow, rotation induces a higher level of the turbulence near the wall at which the main shear vorticity is parallel to the background vorticity (unstable side) and reduces the turbulence near the wall at which these two vectors are antiparallel (stable side). At moderate rotation rates, the cross-stream flow field consists of two large and two small counter-rotating cells. The large cells convect low momentum fluid from the stable side to the unstable side across the central part of the duct. This convective transport displaces the maxima of the axial velocity component towards the side walls and towards the unstable wall as the rotation rate is increased. Turbulence-driven secondary flows at moderate and high rotation rates occur on the unstable side below the corner bisectors. It has been found that, at moderate rotation rates, the streamwise vorticity of these small secondary flows is increased by the presence of the streamwise velocity maxima near the corners. At the highest rotation rate considered, the turbulence level on the stable side is considerably reduced owing to the stabilization of the flow to a Taylor–Proudman regime. This flow structure, which is characterized by the absence of streamwise vorticity in the central part of the duct, is produced by the intensification of the Coriolis-generated vertical x-momentum convective transport.

ACKNOWLEDGMENTS

The support of SEUID (Ministerio de Educación y Cultura, Spain) is gratefully aknowledged. Some of the computations were carried out on Cray supercomputers of the SGI Center at Eagan (MN). We would like to thank S. Gavrilakis, K. Alvelius, and A. Johansson for providing us with the data from their simulations.

APPENDIX

Components of the symmetric tensors P_{ij} and G_{ij} for a fully developed flow in a rotating duct. The dominant terms for the flow conditions simulated in the present study are underlined:

$$P_{ij}^{*}=\begin{pmatrix} -2\left(\underline{\langle u'v'\rangle^{*}\frac{\partial U^{*}}{\partial y}}+\underline{\langle u'w'\rangle^{*}\frac{\partial U^{*}}{\partial z}}\right) & -\left(\begin{array}{l}\langle u'v'\rangle^{*}\frac{\partial V^{*}}{\partial y}+\langle u'w'\rangle^{*}\frac{\partial V^{*}}{\partial z}\\ +\underline{\langle v'^{2}\rangle^{*}\frac{\partial U^{*}}{\partial y}}+\langle v'w'\rangle^{*}\frac{\partial U^{*}}{\partial z}\end{array}\right) & -\left(\begin{array}{l}\langle u'v'\rangle^{*}\frac{\partial W^{*}}{\partial y}+\langle u'w'\rangle^{*}\frac{\partial W^{*}}{\partial z}\\ +\langle v'w'\rangle^{*}\frac{\partial U^{*}}{\partial y}+\underline{\langle w'^{2}\rangle^{*}\frac{\partial U^{*}}{\partial z}}\end{array}\right)\\ - & -2\left(\langle v'^{2}\rangle^{*}\frac{\partial V^{*}}{\partial y}+\langle v'w'\rangle^{*}\frac{\partial V^{*}}{\partial z}\right) & -2\left(\langle v'^{2}\rangle^{*}\frac{\partial W^{*}}{\partial y}+\langle w'^{2}\rangle^{*}\frac{\partial V^{*}}{\partial z}\right)\\ - & - & -2\left(\langle v'w'\rangle^{*}\frac{\partial W^{*}}{\partial y}+\langle w'^{2}\rangle^{*}\frac{\partial W^{*}}{\partial z}\right)\end{pmatrix},$$

$$G_{ij}^{*}=\begin{pmatrix} 2\mathrm{Ro}\langle u'v'\rangle^{*} & \underline{\mathrm{Ro}(\langle v'^{2}\rangle^{*}-\langle u'^{2}\rangle^{*})} & \mathrm{Ro}\langle v'w'\rangle^{*}\\ - & -2\mathrm{Ro}\langle u'v'\rangle^{*} & -\mathrm{Ro}\langle u'w'\rangle^{*}\\ - & - & 0\end{pmatrix}.$$

[1] J. P. Johnston, R. M. Hallen, and D. K. Lezius, ''Effects of spanwise rotation on the structure of two-dimensional fully developed turbulent channel flow,'' J. Fluid Mech. **56**, 533 (1972).
[2] Y. Miyake and T. Kajishima, ''Numerical simulation of the effect of Coriolis force on the structure of turbulence,'' Bull. JSME **29**, 3341 (1986).
[3] D. K. Tafti and S. P. Vanka, ''A numerical study of the effects of spanwise rotation on turbulent channel flow,'' Phys. Fluids A **3**, 642 (1991).
[4] U. Piomelli and J. Liu, ''Large-eddy simulation of rotating channel flows using a localized dynamic model,'' Phys. Fluids **7**, 839 (1995).
[5] R. Kristoffersen and H. Andersson, ''Direct simulations of low-Reynolds-number turbulent flow in a rotating channel,'' J. Fluid Mech. **256**, 163 (1993).
[6] E. Lamballais, M. Lesieur, and O. Métais, ''Effects of spanwise rotation on the vorticity stretching in transitional and turbulent channel flow,'' Int. J. Heat Fluid Flow **17**, 324 (1996).
[7] K. Alvelius, ''Studies of turbulence and its modeling through large eddy-

Downloaded 19 Sep 2001 to 129.16.64.43. Redistribution subject to AIP license or copyright, see http://ojps.aip.org/phf/phfcr.jsp

and direct numerical simulation,'' Ph.D. thesis, Department of Mechanics, Royal Institute of Technology, Stockholm, 1999.
[8]R. V. Madabhushi, and S. P. Vanka, ''Large-eddy simulation of turbulence-driven secondary flows in a square duct,'' Phys. Fluids A **3**, 2734 (1991).
[9]S. Gavrilakis, ''Numerical simulations of low-Reynolds-number turbulent flow through a straight square duct,'' J. Fluid Mech. **244**, 101 (1992).
[10]A. Huser and S. Biringen, ''Direct numerical simulation of turbulent flow in a square duct,'' J. Fluid Mech. **257**, 65 (1993).
[11]J. E. Hart, ''Instability and secondary motion in a rotating channel flow,'' J. Fluid Mech. **45**, 341 (1971).
[12]C. G. Speziale, ''Numerical study of viscous flow in rotating rectangular ducts,'' J. Fluid Mech. **122**, 251 (1982).
[13]C. G. Speziale and S. Thangam, ''Numerical study of secondary flows and roll-cell instabilities in rotating channel flow,'' J. Fluid Mech. **130**, 377 (1983).
[14]W. Kim and S. Menon ''Application of the localized dynamic subgrid-scale model to turbulent wall-bounded flows,'' *35th Aerospace Sciences Meeting & Exhibit*, Reno, NV, 1997, AIAA Paper 97-0210.
[15]U. Piomelli, ''High Reynolds number calculations using the dynamic subgrid-scale stress model,'' Phys. Fluids A **5**, 1484 (1993).
[16]S. Liu, C. Meneveau, and J. Katz, ''On the properties of similarity subgrid-scale models as deduced from measurements in a turbulent jet,'' J. Fluid Mech. **275**, 83 (1994).
[17]P. Emvin, ''The full multigrid method applied to turbulent flow in ventilated enclosures using structured and unstructured grids,'' Ph.D. thesis, Department of Thermo and Fluid Dynamics, Chalmers University of Technology, Gothenburg, 1997.
[18]L. Davidson, ''LES of recirculating flow without any homogeneous direction: A dynamic one-equation subgrid model,'' in *2nd International Symposium on Turbulence Heat and Mass Transfer*, Delft, 1997 (Delft University Press, Delft), pp. 481–490.
[19]A. Sohankar, C. Norberg, and L. Davidson, ''Simulation of three-dimensional flow around a square cylinder at moderate Reynolds numbers,'' Phys. Fluids **11**, 288 (1999).
[20]A. Sohankar, L. Davidson, and C. Norberg, ''Large eddy simulation of flow past a square cylinder: Comparison of different subgrid scale models,'' J. Fluids Eng. **122**, 39 (2000). See also Erratum, J. Fluids Eng. **122**, 643 (2000).
[21]S. Krajnovic and L. Davidson, ''Large-eddy simulation of the flow around a surface-mounted cube using a dynamic one-equation subgrid model,'' in *1st International Symposium on Turbulence and Shear Flow Phenomena*, Santa Barbara, 1999, pp. 741–746.
[22]S.-H. Peng and L. Davidson, ''Numerical investigation of turbulent buoyant cavity flow using large eddy simulation,'' in *3rd International Symposium on Turbulent Heat and Mass Transfer*, 3–6 April 2000, Nagoya, Japan, pp. 737–744.
[23]J. Pallares and L. Davidson, ''Large-eddy simulations of turbulent flows in stationary and rotating channels and in a stationary square duct,'' Department of Thermo and Fluid Dynamics Report No. 00/3, Chalmers University of Technology, Gothenburg, 2000.
[24]J. Kim, P. Moin, and R. Moser, ''Turbulence statistics in fully developed channel flow at low Reynolds number,'' J. Fluid Mech. **177**, 133 (1987).
[25]B. E. Launder, D. P. Tselepidakis, and B. A. Younis, ''A second-moment closure study of rotating channel flow,'' J. Fluid Mech. **183**, 63 (1987).
[26]N. N. Mansour, J. Kim, and P. Moin, ''Reynolds-stress and dissipation-rate budgets in a turbulent channel flow,'' J. Fluid Mech. **194**, 15 (1988).
[27]J. Jeong and F. Hussain, ''On the identification of a vortex,'' J. Fluid Mech. **285**, 69 (1995).
[28]J. Jeong, F. Hussain, W. Schoppa, and J. Kim, ''Coherent structures near the wall in a turbulent channel flow,'' J. Fluid Mech. **332**, 185 (1997).

Downloaded 19 Sep 2001 to 129.16.64.43. Redistribution subject to AIP license or copyright, see http://ojps.aip.org/phf/phfcr.jsp